J. Mech. Phys. Solids 179 (2023) 105389

Contents lists available at ScienceDirect

Journal of the Mechanics and Physics of Solids

journal homepage: www.elsevier.com/locate/jmps

Universal shielding effect of curvature on two interacting cracks

Mengqi Liu [a], Yu Zhen [a], Yi Sun [a], Linghui He [a], Kaijin Wu [a,*], Yong Ni [a,b,*]

[a] CAS Key Laboratory of Mechanical Behavior and Design of Materials, Department of Modern Mechanics, University of Science and Technology of China, Hefei, Anhui 230026, China
[b] State Key Laboratory of Nonlinear Mechanics, Institute of Mechanics, Chinese Academy of Science, 15 Beisihuan West Road, Beijing 100190, China

ARTICLE INFO

Keywords:
Curvature
Fracture
Crack propagation paths
The interaction of multiple cracks
Shielding effect

ABSTRACT

The interaction of approaching cracks plays a crucial role in the formation of complex crack patterns in the mechanics and physics of materials defects. While curvature has been shown to be important in the growth, interaction, and ordering of various defects, its influence on the interactions of multiple cracks remains poorly understood. In this study, we investigate how two approaching cracks interact in curved sheets using an integrated mechanical framework combing experiments, fracture phase-field simulations, and theoretical analysis. Our findings demonstrate that the repulsive and attractive interactions between the two initially parallel cracks are significantly shielded by curvature. This shielding effect arises because curvature alters the stress fields at the crack tips and reduces the initial deflection angle of the crack tips. We observe this effect under different initial crack positions, material properties, and curved configurations, indicating a general role of curvature in controlling the paths and interactions of cracks. This study provides insights into understanding the interaction of approaching cracks, which has implications for fracture and fatigue control.

1. Introduction

In the fields of mechanics and physics of materials defects, curvature has proven to be a key versatile tool to control the assembly, growth and interaction of various defects, which play essential roles in material property and structural safety. For example, curvature can be used to control the self-assembly morphology of defects such as pleats (Irvine et al., 2010), scars (Bausch et al., 2003), wrinkles (Chen et al., 2010; Xu et al., 2016; Zhao et al., 2020; Tobasco et al., 2022; Wang et al., 2023) and lattice defects (Meng et al., 2014; Jiménez et al., 2016; Guerra et al., 2018). The above investigations reveal that curvature can usually promote or inhibit the formation of relevant morphologies and lead to the change of properties, which has aroused great interest of scholars to consider whether curvature can control crack growth and propagation path. (Kamrin, 2017). Wang et al. (2012) reported a 3D helical crack on heterogeneous spindle knots can be controlled by biaxial thermal stresses and unique spindle geometric curvature. Klein and Sharon (2021) presented a new description of a mode I crack as a line distribution of Gaussian curvature and suggested that a proper geometric curvature can be used to avoid fracture. Song et al. (2016, 2017) showed that the crack nucleation and propagation in unzipping of carbon nanotubes is geometry-dependent and the geometrical distortion leads to Griffith strength reduction in graphene membranes. Meanwhile, Feng et al. (2023) reported that the fracture of 2D crystals can be controlled by wrinkling. Furthermore, Mitchell et al. (2017) demonstrated that when thin sheets are draped to a fixed curvature profile, curvature-induced stresses, independent of material

* Corresponding authors.
E-mail addresses: wukaijin@ustc.edu.cn (K. Wu), yni@ustc.edu.cn (Y. Ni).

https://doi.org/10.1016/j.jmps.2023.105389
Received 8 March 2023; Received in revised form 6 July 2023; Accepted 16 July 2023
Available online 24 July 2023

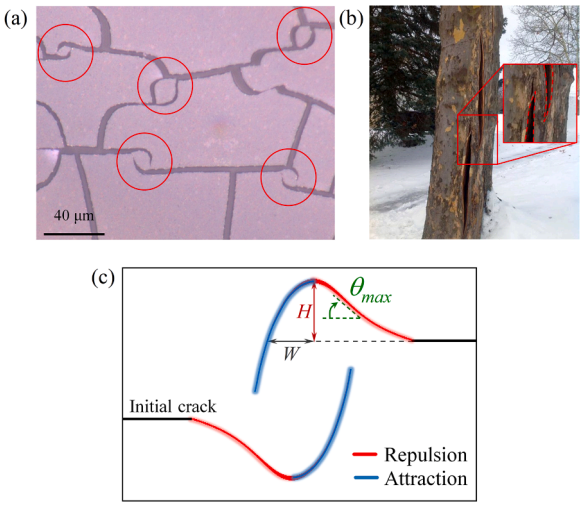

Fig. 1. The interactions between cracks. (a) The interacting crack pairs (highlighted by the red circle) during the volatilization of a silicon oxide film on a flat surface. (b) Frost crack pairs in a tree (highlighted by red dotted lines). Photo credit: Bob Bricault, MSU Extension. (c) Schematic of the geometry of the crack pair composed of the initial repulsion segments and subsequent attraction segments, where the maximum inclination angle θ_{max} and the aspect ratio H/W characterize the degree of crack repulsion and attraction, respectively.

parameters, can be used to stimulate or suppress the growth of a single crack and steer or arrest its propagation. The above research has confirmed that the propagation path of a single crack can be controlled by adjusting the curvature.

However, failures and progressive damages are often related to interactions of multiple cracks. The interaction between multiple cracks will lead to physically important effects, for instance, the impact of interactions on individual cracks, particularly on the stress intensity factors (SIFs), and the effective elastic properties of solids with many cracks (Kachanov, 1993). Interactions can produce a variety of phenomena, stress shielding (decrease of SIFs) and stress amplification (increase of SIFs), coupling of the normal and shear modes (Han et al., 2019), and it will also lead to stiffness degradation and anisotropy development of the system with multiple cracks (Zeng and Wei, 2016). In addition, observed in the laboratory and nature (e.g. Fig. 1a and 1b), the propagation and the interaction of multiple cracks may exhibit complex and ordered crack patterns under different load types (Yuse and Sano, 1993; Marthelot et al., 2014, 2015; Goehring et al., 2015; Ball, 2016; Martins et al., 2018), which are obviously of crucial importance for the safety design and fracture control of thin films (Liu et al., 2022), flexible electronics (Rogers et al., 2010) and engineering materials (Kang et al., 2014). Under mode III loading, like pulling away a strip of adhesive tape, the interaction between two tearing cracks in a thin sheet is attractive, which always leads to a pointy shape. Hamm et al. (2008) showed that the detached flaps have perfect triangular shapes with a well-defined vertex angle. Bayart et al. (2011) and Brau (2014) considered the case of no adhesion between the sheet and the substrate, and showed that the crack paths are no longer linear, which forms a tongue-like shape. It is remarkable that Kruglova et al. (2011) showed that the interaction between two tearing cracks in adhesive thin films can be attractive or repulsive, depending on their curvature and mediated by adhesion. Besides, dominated by curvature-dependent bending energy, the propagation of multiple tearing cracks induced by indenting a thin, elastic, brittle sheet with a rigid cone can be changed from a symmetrically radial path to logarithmic spiral paths (Fuentealba et al., 2016). Under mode I & II loading, a straight-sided buckle-delamination in film-substrate systems can be seen as two interface cracks mediated by buckling, which may exhibit various propagation paths. Ni and Soh (2014) investigated the growth mechanisms of nonlinear buckle-delamination patterns, ranging from straight-sided to telephone cord and network-like blisters. The interaction between buckle-delaminations can be complex and can lead to the coalescence behaviors of the buckles, resulting in the formation of network-like blisters. Yu et al. (2013) experimentally reported the rich coalescence behaviors and morphological evolutions of telephone cord buckles in $SiAlN_x$ films. In a study by Coupeau et al. (2019), it was demonstrated that two straight-sided buckle-delaminations exhibit an apparent attraction towards each other once their two propagation fronts cross. It indicates that such crack interaction becomes more complex under the influence of stress anisotropy and the interaction between the film and the substrate. The interaction between two initially parallel cracks under mode I loading has received considerable attention in the past decades, primarily due to its idealized configuration for studying the interaction and coalescence of multiple cracks. The pair of cracks usually produces a universal fracture path known as En-Passant cracks (Kranz, 1979), where the cracks initially curve away from each other before turning sharply inwards and attracting until coalescence, forming a hook-shaped path with repulsive and attractive segments (Fig. 1c). This universal behavior originates from the appearance of mixed mode interactions caused by a disturbed symmetry and the stress field in the vicinity of crack tips being modified by the presence of the other adjacent cracks (Ghelichi and Kamrin, 2015; Koivisto et al., 2016). There have been a lot of studies on this aspect. For example, Melin (1983) showed the defect-induced instability of two collinear cracks in a flat plate. Seelig and Gross (1999) performed a numerical investigation on the interaction and branching of dynamic cracks. Fender et al. (2010) found that the two approaching cracks can form a universal fragment shape with an aspect ratio of 2:1. Furthermore, Dalbe et al. (2015) observed the transition from repulsive to attractive interaction of cracks in a plastic sheet. Schwaab et al. (2018) performed theoretical and numerical works to reveal the multiscale behavior of the

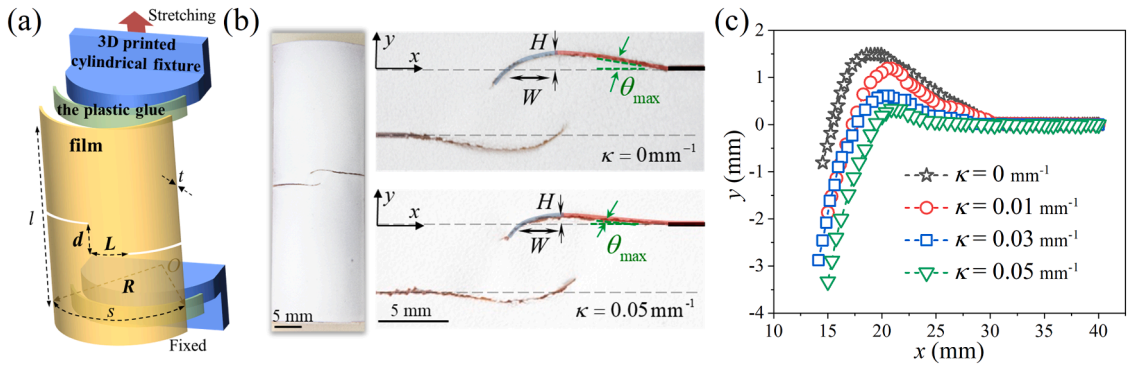

Fig. 2. Experimental investigations for the effects of curvature on the interaction of two parallel and offset cracks. (a) A schematic diagram for a curved shell (R is the radius of curvature) with two initial notches separated by vertical d and horizontal L distances under mode I loading, where the thin polyimide film is firmly stuck to the 3D printed curved heads by the plastic glue with high adhesive strength. (b) A typical 3D experimental morphology (left) for cracks on a curved film with initial $L = 20$ mm and $d = 4$ mm, and the comparison of crack morphologies on flat and curved samples (right). (c) Experimental curves of crack trajectories under diverse curvature κ (Here, to better compare the crack paths under diverse curvature, we converted the coordinates of the cracks on the curved surface to those on the plane, see Appendix B).

repulsive-attractive transition. Yet, current studies mainly focus on the interaction of two mode I cracks in flat sheets. Whether the promotion or inhibition caused by the interaction between curvature and cracks will be coordinated or countered? It remains elusive to understand how curvature affects the interaction and entire propagation path of cracks, which is critical for the future design of crack-resistant structures.

For a single crack, there have been some theoretical studies on the solution for the stress distribution around the tip of a slightly curved crack (Cotterell and Rice, 1980) and a crack on the curved surface (Folias, 1969). In recent years, remarkable theoretical investigations have advanced the research on crack interaction. Liu and Wei (2021) provided the close-form solution works for arbitrarily sized kinked cracks. Vattré (2022) got the general full-field solutions about the fracture problem of multiple branched crack arrays in anisotropic bimaterials. Yao and Zhang (2022a,b) provided a generalized and more accurate solution to the annular contact problem or the combo crack problem. However, such efforts are not enough to obtain the spatiotemporal evolution process and interaction of crack-tip stress field in multiple approaching cracks. Fortunately, phase field modeling of fracture has been shown as an efficient computational technique that can simulate topologically complex fracture processes (Francfort and Marigo, 1998; Bourdin et al., 2000, 2008; Pons et al., 2010; Wu et al., 2020). It opens a way for us to comprehensively investigate the effects of curvature on the interaction of multiple approaching cracks.

In this work, combining experimental, numerical and theoretical studies, we investigated the propagation path and interaction of two approaching cracks on curved structures, and found that curvature can significantly shield the repulsive and attractive interactions between cracks. This seems to be confirmed by the frost cracks formed by expansion or contraction on the curved surface of the tree (Fig. 1b), where the interaction between cracks is relatively weak compared with the plane situation (Fig. 1a). The remainder of this paper is structured as follows. In Section 2, we carried out systematic experiments to study the effect of curvature on the interaction between cracks. In Section 3, we employed the phase-field fracture method to simulate the crack propagation path on the curved structure and analyzed the von Mises stress distribution at the crack tip during the propagation process. In Section 4, a semi-theoretical analysis method including fracture mechanics theory and finite element method is used to analyze the effect of curvature on the initial deflection angle of crack tip. The main conclusion is summarized in Section 5.

2. Experimental observation

2.1. Experimental setup

To study the effect of curvature on the interaction between two cracks, we apply a mode I loading to an open cylindrical elastic shell with a pair of offset notches (Fig. 2a). The material of the shell is a thin polyimide film with axial length $l = 80$ mm, arc length $s = 40$ mm, thickness $t = 50$ μm, elastic modulus $E = 1.5$ GPa and fracture toughness $G_c = 35$ N/mm (see Appendix A). To start, we cut a pair of offset notches separated by different horizontal distances L and vertical distances d, symmetric to the center of the polyimide film. The cut film was firmly adhered to 3D printed cylindrical fixtures with a certain radius of curvature R by a plastic glue, which has strong enough adhesive strength between the film and the fixture to avoid delamination and ensure the crack propagation. For the ultrathin curved film ($t/s \sim 10^{-3}$) with small curvature ($R/s \sim 1$), its bending stiffness is in the order of $\sim t^3$, and thus the curved films have extremely small bending energy and remain in a stress-free state (Wang et al., 2020). To apply a mode I loading on the curved film and keep the initial curved configuration, two 3D printed fixtures were fixed to the Material Test System (MTS criterion 43, MTS System Company), where the centers of the upper and lower fixtures are in a vertical line, and the top fixture is axially stretched with a loading rate of 0.1 mm/min. It's worth a mention that due to the errors of uniaxial loading conditions and the local nonlinear large deformation of film in experiments, there are some differences between local curved geometries and initial curved configuration, which have

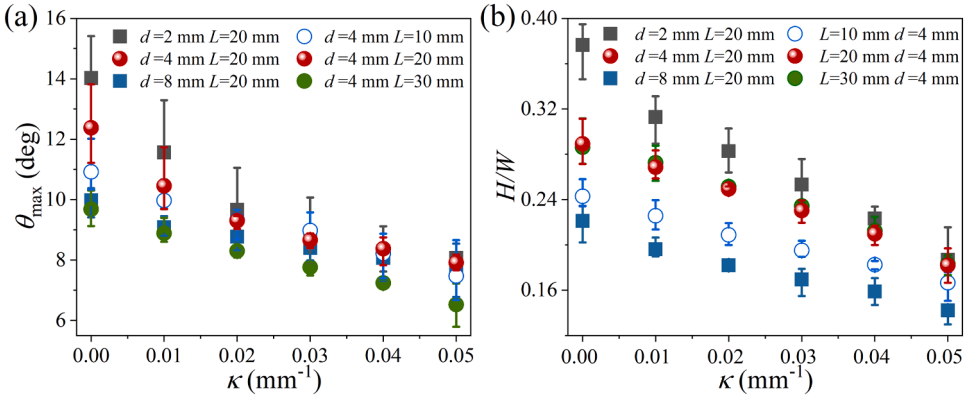

Fig. 3. Experimentally measured θ_{max}(a) and H/W (b) as functions of the curvature κ under different values of d and L.

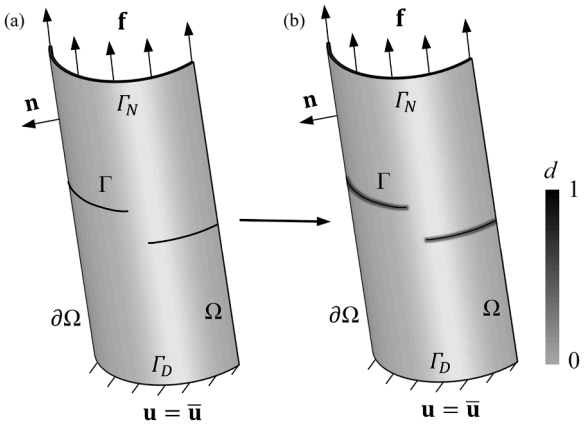

Fig. 4. (a) The schematic illustration of a body with a pair of sharp cracks. (b) Representation of a pair of discrete cracks by phase field d.

negligible influences on the shielding effect of curvatures on crack interactions. As shown in Fig. 2b, to characterize the final interacting crack trajectories, we recorded the 3D crack morphology by a camera, and we removed the final postmortem films with cracks from the 3D printed fixtures and flatten them to measure the geometries of cracks, including maximum the inclination angle θ_{max} and the aspect ratio H/W.

2.2. *The shielding effect of curvature on the interaction of cracks*

As shown in Fig. 2b, the crack pair trajectories on curved samples are composed of the initial repulsive segments and subsequent attractive segments, which are similar to those on flat samples. Interestingly, we observed that compared with the crack pairs on flat samples, the crack pairs on curved samples show weaker repulsive and attractive interaction, with smaller θ_{max} and H/W characterizing the amplitude of the attraction and repulsion. To quantitatively analyze the effects of curvature on the interaction between a pair of cracks, we plotted the crack trajectories of samples with different curvature κ in the x-y coordinate system shown in Fig. 2c (see Appendix B), in which the crack trajectories depend strongly on the curvature, and the repulsive and attractive interaction are significantly shielded when the curvature increases.

Furthermore, systematic experimental results show that the angle θ_{max} corresponding to the maximum slope of the initial repulsion segments decreases with the curvature, indicating the shielding effect of curvature on the repulsive interaction of the crack pair (Fig. 3a). Meanwhile, the aspect ratio H/W of subsequent attractive segments also decreases with the curvature, which indicates that the curvature can also significantly shield the attractive interaction between a pair of cracks (Fig. 3b). The shielding effects of curvature on the interaction of the crack pairs remain valid under different initial horizontal distances L and vertical distances d. In addition, we found that for the crack pairs on a flat sheet, θ_{max} and H/W are independent of L and decrease with d, with weaker repulsion and attraction when the initial vertical crack separation d increases, which is consistent with the results reported by Dalbe et al. (2015). With the increase of curvature, both θ_{max} and H/W become independent of d due to the significant shielding effect of curvature on the repulsion and attraction between a pair of cracks.

3. Numerical analysis

3.1. Phase-field fracture method

To further unveil the shielding effect of curvature on the repulsion and attraction between the crack pairs, we simulated complete crack trajectories using a fracture phase-field method. The approach introduces a regularized sharp crack taken into account by an auxiliary scalar damage variable between zero and one, which connects broken and unbroken regions, thus turning the discontinuous system into a continuous system (Fig. 4a and 4b). Once its value reaches one the material is fully broken, and both its stiffness and stress are reduced to zero. The variable varies continuously between the damaged and undamaged regions, which can be described as an exponential function from Miehe et al. (2010) to represent a regularized or diffusive crack topology, $d(\boldsymbol{x}) = e^{-|\boldsymbol{x}|/l_0}$. l_0, an internal characteristic length scale parameter, controls the width of the diffusive crack topology. The ideal sharp crack can be recovered within the limit of $l_0 \to 0$. Therefore, the total energy can be composed of three parts: the elastic energy, the fracture energy, and the external potential energy by external loads:

$$\Pi(\mathbf{u}, \mathbf{b}, \mathbf{f}, d, \nabla d) = \int_{\Omega} \psi^e(\boldsymbol{\varepsilon}^e(\mathbf{u}), d)\mathrm{d}\Omega + \int_{\Omega} \psi^f(\nabla d, d)\mathrm{d}\Omega + \int_{\Omega/\partial\Omega} \psi^{ext}(\mathbf{u}, \mathbf{b}, \mathbf{f})\mathrm{d}\Omega \,/\, \partial\Omega, \tag{3.1}$$

where $\mathbf{u}$ is the displacement vector, $\boldsymbol{\varepsilon}^e(\mathbf{u})$ is the elastic strain tensor, d is the so-called phase field scalar parameter, $\mathbf{f}$ is the surface force on the boundary $\partial\Omega$, $\mathbf{b}$ is a body force acting on the body Ω. The isotropic elastic energy function $\psi^e(\boldsymbol{\varepsilon}^e)$ associated with the undamaged elastic solid can be written as:

$$\psi^e(\varepsilon^e) = \frac{1}{2}(\boldsymbol{\varepsilon}^e)^{\mathrm{T}} : \mathbf{C}_0 : \boldsymbol{\varepsilon}^e = \frac{1}{2}\lambda[tr(\boldsymbol{\varepsilon}^e)]^2 + \mu tr\left[(\boldsymbol{\varepsilon}^e)^2\right], \tag{3.2}$$

where $\mathbf{C}_0$ is the unbroken material stiffness tensor, $\lambda = E\nu/[(1+\nu)(1-2\nu)]$ and $\mu = E/[2(1+\nu)]$ are Lame constants in the case of isotropic elasticity, E is Young's modulus, ν is Poisson's ratio. The total strain tensor is expressed as the displacement gradient $\nabla\mathbf{u}$ under the assumption of small strains: $\boldsymbol{\varepsilon}^e = (\nabla\mathbf{u} + (\nabla\mathbf{u})^{\mathrm{T}})/2$. To ensure that the crack is only driven by tension and avoid the influence of the unphysical load-bearing capacity of the cracked regions, the elastic strain tensor is divided into the tensile part and compressive part:

$$\boldsymbol{\varepsilon}^e = \boldsymbol{\varepsilon}^{e+} + \boldsymbol{\varepsilon}^{e-}. \tag{3.3}$$

After considering the degradation of energy due to fracture, the total elastic energy density depending on the phase field $\psi^e(\boldsymbol{\varepsilon}^e, d)$ can be expressed as follows:

$$\psi^e(\boldsymbol{\varepsilon}^e, d) = \mathrm{g}(d)\psi^{e+}(\boldsymbol{\varepsilon}^e) + \psi^{e-}(\boldsymbol{\varepsilon}^e), \tag{3.4}$$

$$\psi^{e+}(\boldsymbol{\varepsilon}^e) = \frac{\lambda}{2}\langle tr(\boldsymbol{\varepsilon}^e)\rangle_+^2 + \mu tr\left[(\boldsymbol{\varepsilon}^{e+})^2\right], \tag{3.5}$$

$$\psi^{e-}(\boldsymbol{\varepsilon}^e) = \frac{\lambda}{2}\langle tr(\boldsymbol{\varepsilon}^e)\rangle_-^2 + \mu tr\left[(\boldsymbol{\varepsilon}^{e-})^2\right], \tag{3.6}$$

where $\mathrm{g}(d) = (1-d)^2 + \delta$ is the degradation function, representing the reduction of stiffness due to the crack in the material, δ is a model parameter for avoiding numerical singularities. The operators $\langle\cdot\rangle_+$ and $\langle\cdot\rangle_-$ are defined as: $\langle\cdot\rangle_+ = (\cdot + |\cdot|)/2$ and $\langle\cdot\rangle_- = (\cdot - |\cdot|)/2$. The fracture energy ψ^f depends on the critical energy release ratio G_c and the crack surface density per unit volume of the solid $\gamma(d, \nabla d)$:

$$\psi^f(\nabla d, d) = G_c\gamma(d, \nabla d) = G_c\left(\frac{1}{2l_0}d^2 + \frac{l_0}{2}|\nabla d|^2\right). \tag{3.7}$$

Then the total Lagrange energy functional can be expressed as follows:

$$\Pi = \int_{\Omega}[\mathrm{g}(d)\psi^{e+}(\boldsymbol{\varepsilon}^e) + \psi^{e-}(\boldsymbol{\varepsilon}^e)]\mathrm{d}\Omega + \int_{\Omega} G_c\left(\frac{1}{2l_0}d^2 + \frac{l_0}{2}|\nabla d|^2\right)\mathrm{d}\Omega + \int_{\Omega}\mathbf{u}\cdot\mathbf{b}\mathrm{d}\Omega + \int_{\partial\Omega}\mathbf{u}\cdot\mathbf{f}\mathrm{d}\partial\Omega. \tag{3.8}$$

To ensure the irreversibility condition ($\dot{d} \geq 0$) to prevent crack healing, the local history field H defined as the maximum strain energy contributed by tensile strain components has been introduced:

$$H(\mathbf{r}, t) = \max_{\tau\in[0,t]}\psi^{e+}(\mathbf{r}, \tau). \tag{3.9}$$

Thus, the total Lagrange energy functional can be written by:

$$\Pi = \int_{\Omega}[\mathrm{g}(d)H + \psi^{e-}(\boldsymbol{\varepsilon}^e)]\mathrm{d}\Omega + \int_{\Omega} G_c\left(\frac{1}{2l_0}d^2 + \frac{l_0}{2}|\nabla d|^2\right)\mathrm{d}\Omega + \int_{\Omega}\mathbf{u}\cdot\mathbf{b}\mathrm{d}\Omega + \int_{\partial\Omega}\mathbf{u}\cdot\mathbf{f}\mathrm{d}\partial\Omega. \tag{3.10}$$

The following governing equations are derived by taking the variation of the total energy functional, which means that the first

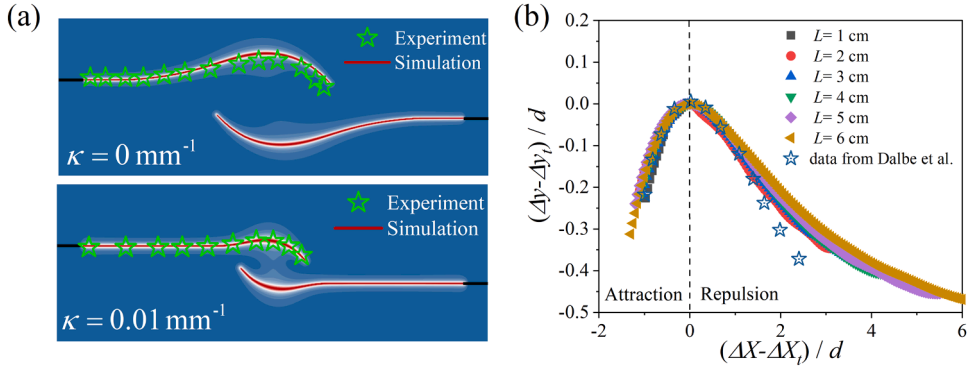

Fig. 5. Verification of the phase field model. (a) Comparison of simulated and experimental crack morphologies on flat and curved shells, respectively. (b) Comparison of simulated crack morphologies with the experimental data of Dalbe et al. (2015) on flat shells.

variation of the total Lagrange energy function Π with respect to **u** and d equals to zero:

$$\begin{cases} \nabla \cdot \boldsymbol{\sigma} + \mathbf{b} = 0 & in\ \Omega \\ \left(\dfrac{2l_0 H}{G_c} + 1\right) d - l_0^2 \nabla^2 d = \dfrac{2l_0 H}{G_c} & in\ \Omega \\ \boldsymbol{\sigma} \cdot \mathbf{n} - \mathbf{f} = 0 & on\ \Gamma_N \\ \mathbf{u} - \bar{\mathbf{u}} = 0 & on\ \Gamma_D \\ \nabla d \cdot \mathbf{n} = 0 & in\ \ \Gamma \end{cases}, \tag{3.11}$$

where $\boldsymbol{\sigma} = (1-d)^2 \partial \psi^{e+}(\boldsymbol{\varepsilon}) / \partial \boldsymbol{\varepsilon} + \partial \psi^{e-}(\boldsymbol{\varepsilon}) / \partial \boldsymbol{\varepsilon}$ is the Cauchy stress tensor.

In Eq. (3.11), the stiffness only degrades in the direction of tensile load, where only the tensile energy ψ^{e+} is degraded and drives the evolution of the crack field d. This leads to that the fully broken region ($d = 1$) can still support the mechanical loads in other directions, which is inconsistent with fracture mechanics (Jeong et al., 2018). In this work, due to the asymmetry of two approaching cracks on curved structures, the mixed mode fracture with both tensile and shear loading occurs at the crack tips. Therefore, we developed the hybrid phase field model proposed by Ambati et al. (2015) to track the trajectory and interaction of two approaching cracks bearing combined tensile and shear loads at crack tips. Considering the degradation of stiffness in all directions, the Cauchy stress tensor **σ** in Eq. (3.11) is modified as:

$$\boldsymbol{\sigma} = (1-d)^2 \partial \psi^{e}(\boldsymbol{\varepsilon}) / \partial \boldsymbol{\varepsilon}, \tag{3.12}$$

Meanwhile, to prevent crack surface interpenetration, a constraint was added:

$$\forall x : \psi^{e+} < \psi^{e-} \Rightarrow d \equiv 0. \tag{3.13}$$

Therefore, the governing equation for the hybrid phase field model is written as:

$$\begin{cases} \nabla \cdot \boldsymbol{\sigma} + \mathbf{b} = 0 & in\ \Omega \\ \left(\dfrac{2l_0 H}{G_c} + 1\right) d - l_0^2 \nabla^2 d = \dfrac{2l_0 H}{G_c} & in\ \Omega \\ \boldsymbol{\sigma} \cdot \mathbf{n} - \mathbf{f} = 0 & on\ \Gamma_N \\ \mathbf{u} - \bar{\mathbf{u}} = 0 & on\ \Gamma_D \\ \nabla d \cdot \mathbf{n} = 0 & in\ \Gamma \\ \forall x : \psi^{e+} < \psi^{e-} \Rightarrow d \equiv 0 \end{cases}, \tag{3.14}$$

where $\boldsymbol{\sigma} = (1-d)^2 \partial \psi^{e}(\boldsymbol{\varepsilon}) / \partial \boldsymbol{\varepsilon}$ is the Cauchy stress tensor.

In the simulation, we utilized the explicit staggered scheme, in which the displacement and the crack field are computed alternately during the calculation iteration. We implemented the crack field solver for the quasi-static fracture of elastic solid in the commercial software ABAQUS by fixed mesh (see Appendix C), which is an adaptation of a procedure proposed by Molnár and Gravouil (2017).

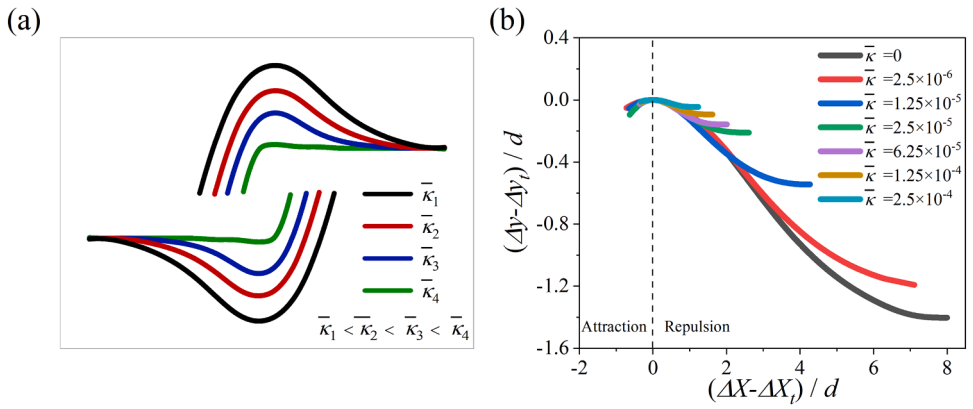

Fig. 6. (a) Simulated crack trajectories under different curvature. (b) The crack trajectories under different curvature cannot collapse into a curve.

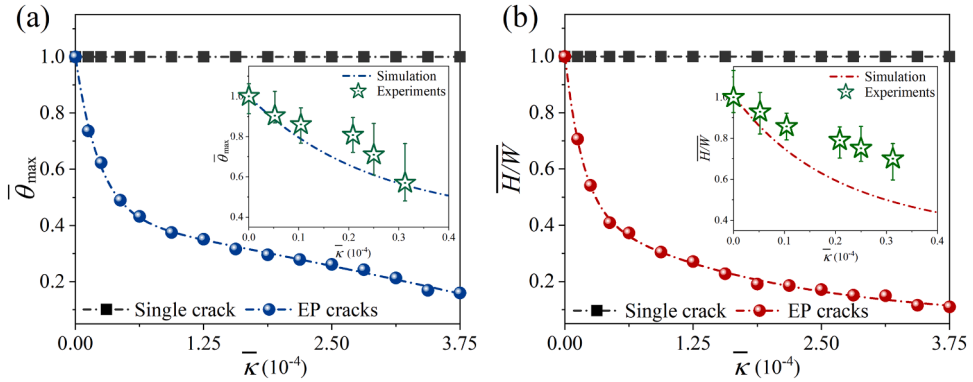

Fig. 7. Phase-field simulations for the interaction of the crack pair on the curved shell. (a-b) Evolutions of the dimensionless geometric parameters $\bar{\theta}_{\max}$ (a) and $\overline{H/W}$ (b) for the single crack and the crack pair, respectively, as functions of $\bar{\kappa}$, and insets show the comparison of experiments and simulations.

3.2. The validation of the method

To verify the correctness of our phase-field model, we compared the simulation results with the experimental results. First of all, under different curvature ($\kappa = 0$ mm^{-1} and $\kappa = 0.01$mm^{-1}), we compared the simulated results with the crack paths obtained in our previous experiments (Fig. 5a). It can be seen that the simulated trajectories of a pair of cracks on flat sheets and curved sheets are in good agreement with experiments, where the trajectories on curved sheets were flattened in order to compare with that on flat sheets (see Appendix B). Meanwhile, it's worth mentioning that there may be some differences between the crack trajectories obtained from simulations and experiments, due to the influences of out-of-plane deformations and boundary conditions in experiments. In addition, we also compared the simulation results under different L when the curvature $\kappa = 0$ mm^{-1} with the experimental data of Dalbe et al. (2015) (Fig. 5b). ΔX and ΔY correspond to the horizontal and vertical distances between the two crack tips. $\Delta y = \Delta Y - \Delta Y_m$ with $\Delta Y_m = d + \Delta u$ measures the distance between the axes of the two cracks in the deformed state. Δu is the elastic tensile elongation of the samples on the distances measured in the deformed state. ΔX_t and Δy_t are the relative distance between the corresponding two crack tip points when Δy reaches the maximum value in the crack pair propagation. The simulation results show that various crack trajectories collapse on a single master curve and they do not depend on L, which is coincided with the experimental results of Dalbe et al. (2015). To sum up, it can be proved that our model can accurately capture the propagation process of two interacting initially parallel cracks under different curvature.

3.3. The effect of curvature on crack propagation paths

We simulated complete crack trajectories using the hybrid fracture phase-field method, where the geometric conditions and material properties in simulations are consistent with those in experiments. In order to better represent the relationship between various parameters, we introduced dimensionless parameters $\bar{\kappa} = t^2/Rd$, $\overline{H/W} = (H/W)/(H_p/W_p)$ and $\bar{\theta}_{\max} = \theta_{\max}/(\theta_{\max})_p$, where $(\cdot)_p$ represents the parameter values of cracks on plane. The simulated crack trajectories under different curvature show that the amplitude of the deviation between the cracks is reduced as the curvature increases, reflecting the shielding effects of curvature on the repulsive and

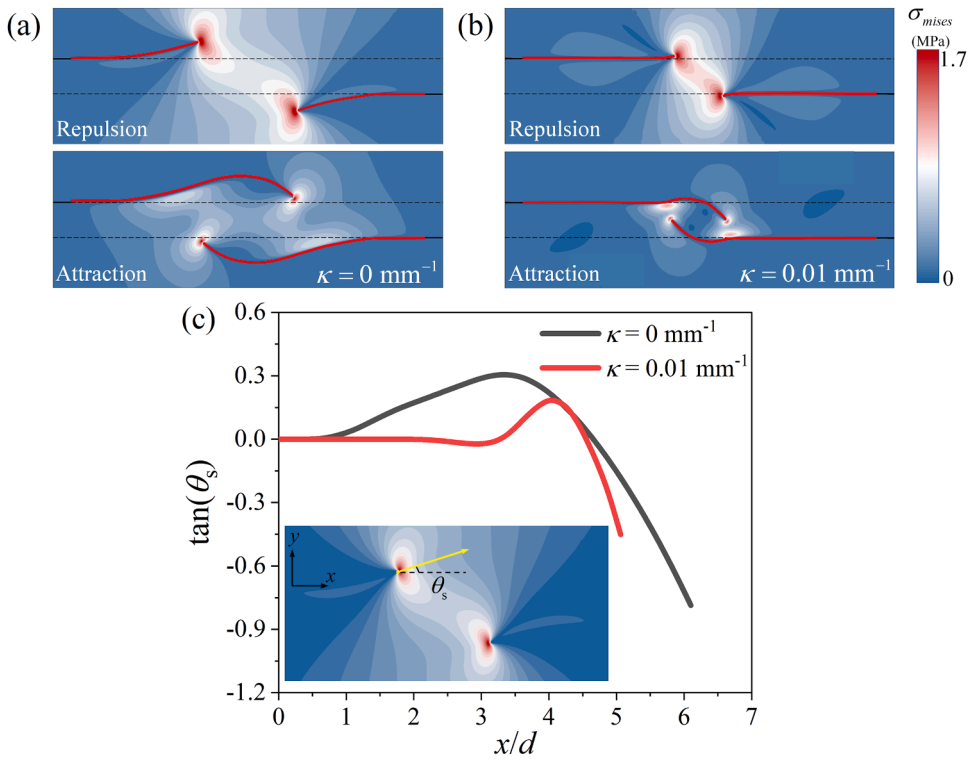

Fig. 8. The von Mises stress field at the tips of cracks on (a) flat and (b) curved shells in the repulsive stage and the attractive stages, respectively. (c) The evolution of the maximum principal stress direction θ_s at crack tips as the crack propagates on flat and curved sheets.

attractive interaction of a pair of cracks (Fig. 6a). In addition, we found that the crack trajectories under different curvature cannot collapse into a single main curve (Fig. 6b), which indicates that the curvature breaks the law found in the case of plane (Fig. 5b).

Furthermore, more detailed simulated results show that both repulsion angle $\overline{\theta}_{\max}$ and the aspect ratio $\overline{H/W}$ decrease with the curvature (Fig. 7a and 7b), which further indicates that the curvature can shield the repulsion and attraction between a pair of cracks. The insets in Fig. 7a and 7b show that the simulated shielding trends of $\overline{\theta}_{\max}$ at repulsive stages and $\overline{H/W}$ at attractive stages are consistent with the results in the experiments. There are some numerical errors between experiments and calculations due to the errors of uniaxial loading conditions, the local nonlinear curved deformations, and material properties in experiments. In addition, for the propagation of a single crack under different $\bar{\kappa}$, the crack path is a straight line without repulsion and attraction and both $\overline{\theta}_{\max}$ and $\overline{H/W}$ are equal to one (Fig. 7a and 7b), which demonstrates that the shielding effect of curvature on the interaction between a pair of cracks cannot be derived by a superposition of the interaction between the single crack and the curvature.

3.4. *The effect of curvature on the von Mises stress fields at crack tips*

In Fig. 8a and 8b, we plotted the von Mises stress fields in the vicinity of crack tips at repulsive and attractive stages as the crack grows on flat and curved sheets under the same displacement, respectively. Initially, the line of maximum tension stress is aligned with the mode I loading because the two cracks are relatively far apart and do not interact with each other, allowing the crack paths to remain straight and parallel. As the two cracks interact with each other, each crack modifies the stress field at the tip of its opposing crack, and the line of maximum tension stress within the central region connects the crack tips and rotates under locally mixed mode I and II loading. At the repulsive stage, the cracks on the plane interact with each other earlier, which leads to the stress field acting on a longer range (Fig. 8a). For the cracks on curved sheets, two cracks start to repulse each other until they are very close to each other, the stress field acts on a narrow range and the amplitude of stress is larger (Fig. 8b). In this case, the amplitude of the deviation in repulsive segments is reduced, reflecting the shielding effect of curvature on the repulsive interaction of cracks. At the attractive stage of cracks on the flat sheet (Fig. 8a), the amplitude of stress is larger and the stress field acts on a longer range. In contrast, for cracks on curved sheets (Fig. 8b), the intensity of the singular stress field ahead of the crack tip is smaller and the stress field acts on a narrow range, which leads to a smaller aspect ratio of subsequent attractive segments, reflecting the shielding effect of curvature on the attractive interaction of cracks. Further, we quantitatively analyzed the evolution of the maximum principal stress direction θ_s at crack tips as the crack propagates on flat and curved sheets (Fig. 8c), where the sign of θ_s indicates repulsive ($\theta_s > 0$) and attractive ($\theta_s < 0$) stages. Results show that as the cracks propagate, the value of $\tan(\theta_s)$ first increases from zero to a maximum value and then decreases to zero, which corresponds to the crack repulsive stage, and then $\tan(\theta_s)$ becomes negative and decreases, which corresponds to the crack

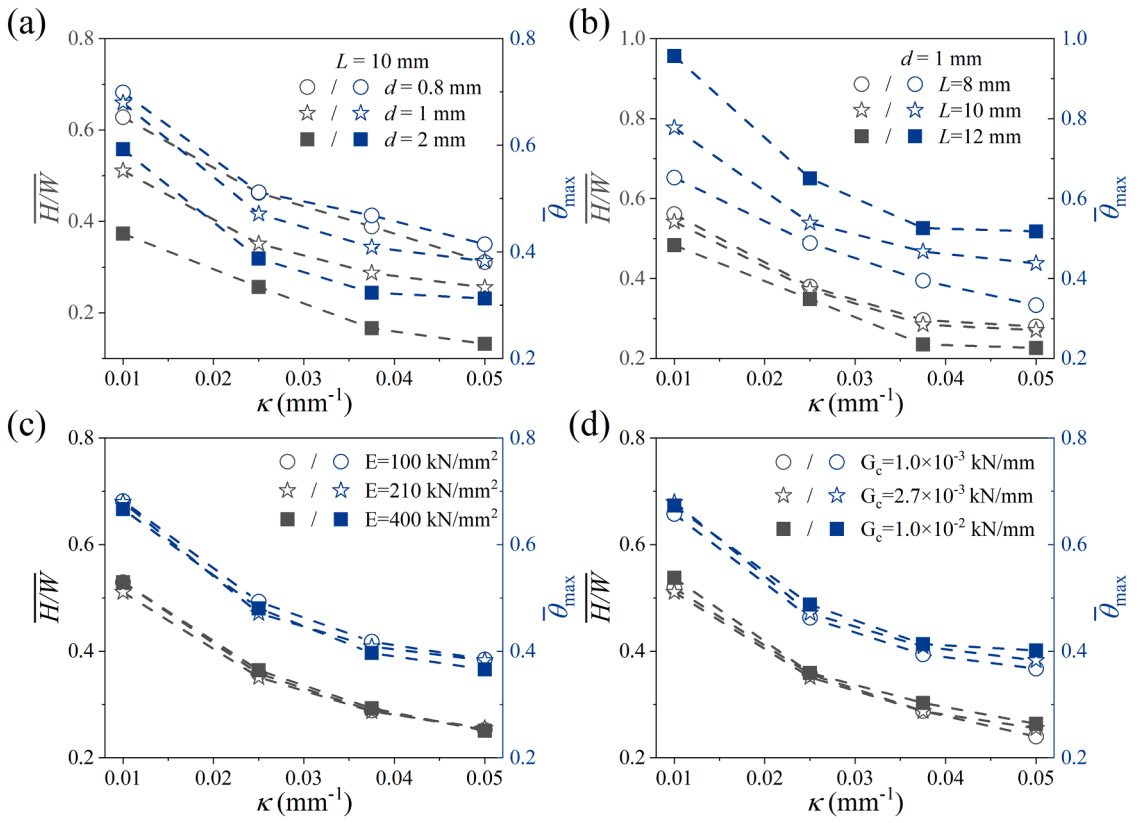

Fig. 9. The universality of the shielding effect of curvature. Effects of (a) the axial distance of the crack pair d, (b) the lateral distance of the crack pair L, (c) the elastic modulus E, and (d) the fracture toughness G_c on the geometries $\overline{\theta}_{max}$ and $\overline{H/W}$ of two interacting cracks.

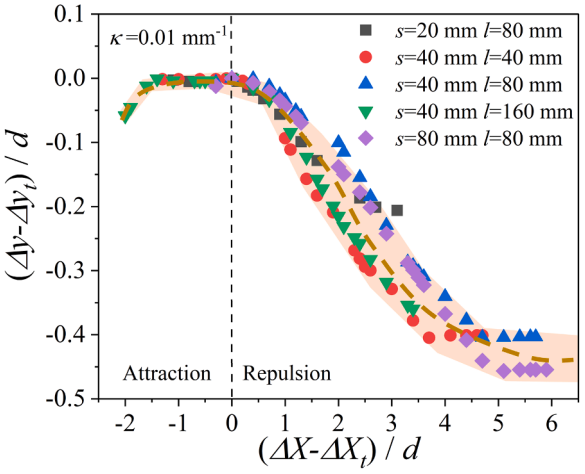

Fig. 10. The normalized crack trajectories under different geometric sizes at a same curvature.

attractive stage. Meanwhile, the values of $\tan(\theta_s)$ for cracks on curved shells are significantly lower than that for cracks on flat sheets, which further reflects the shielding effect of curvature on the repulsive and attractive interactions between a pair of cracks. Therefore, curvature can strongly modify the distribution and intensity of the singular stress field ahead of the crack tip, and as a consequence, lead to a shielding of the repulsion and attraction between a pair of cracks.

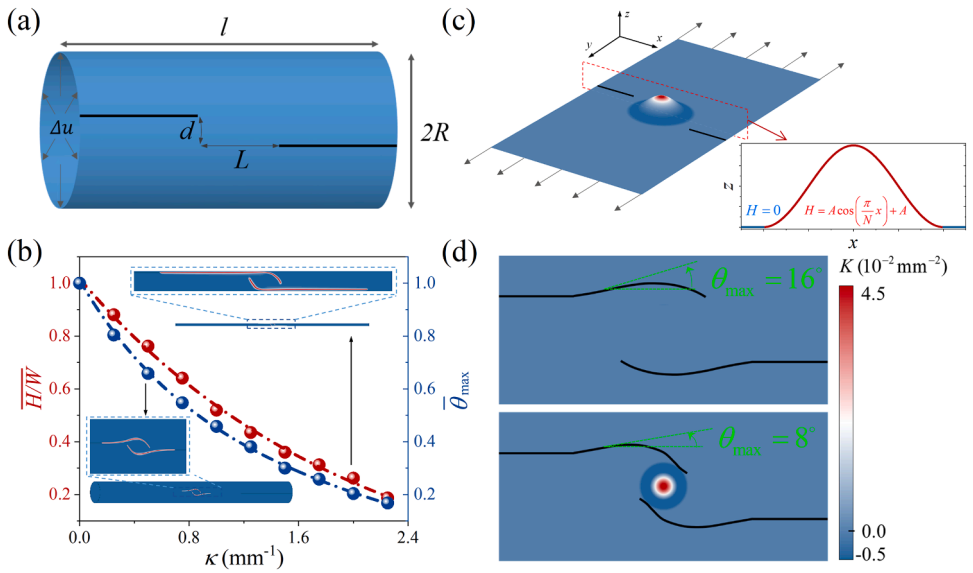

Fig. 11. Shielding effects of curvature on the interaction of the crack pair on different curved configurations. (a) The simulated model of cracks on the close cylindrical shell with two initial notches separated by vertical d and horizontal L distances submitted to internal radial expansion. (b) Evolutions of the aspect ratio $\overline{H/W}$ and the maximum repulsive angle $\overline{\theta}_{\max}$ under different curvature κ. (c) The simulated model of the crack pair around a bump with Gaussian curvature distributions. (d) Simulated trajectories for the crack pair on plane and around a bump.

3.5. *The universality of the shielding effect*

In order to prove the universality of the shielding effect of curvature on the interaction between cracks, we analyzed the influence of geometry parameters, such as the spacing of crack pairs d and L, and the material parameters, such as elastic modulus E and fracture toughness G_c. More detailed fracture phase-field simulations show that both repulsive angle $\overline{\theta}_{\max}$ and the aspect ratio $\overline{H/W}$ decrease with the curvature under different initial horizontal d and vertical L distances between crack tips (Fig. 9a and 9b), which are consistent with the results of our experiments (Fig. 3a and 3b). Meanwhile, it is worth noting that in this work, we mainly focus on the effect of curvature on two interacting cracks. As discussed by previous works (Dalbe et al., 2015; Schwaab et al., 2018), the interaction between cracks becomes weaken as the d increases, and there are no interactions between two cracks when the d exceeds a critical value, and thus the influence of curvature on crack interactions will disappear. In addition, the material properties do not influence the shape of the final trajectory in the elastic brittle case with different curvature (Fig. 9c and 9d). This point of view is consistent with Schwaab (2018), where E and G_c affect the strain energy and the crack propagation speed, but not its shape. Therefore, the shielding effect of curvature on the repulsion and attraction between a pair of cracks remains valid, in a wide range of the initial crack positions and material properties. Besides, under different geometric dimensions (l and s), the normalized crack paths collapse approximately near a same curve (the yellow dotted line in Fig. 10) under $\kappa = 0.01\text{mm}^{-1}$, which reveals that geometric size does not affect the shielding effect of curvature on the crack pair.

In addition, with the aim of demonstrating the universality of the shielding effect, we further explored the propagation of cracks on different curved configurations through phase-field simulation. Typically, as shown in Fig. 11a, we simulated the entire crack pair trajectories on a close cylindrical shell with $l = 80$ mm, $L = 12$ mm, $d = 1$ mm, $E = 1.5$ GPa and $G_c = 35$ N/mm, where the uniformly distributed displacements were imposed outward along the normal direction of the inner surface. The insets in Fig. 11b show that the trajectories of cracks on close cylindrical shells are also composed of the initial repulsive segments and subsequent attractive segments, and the amplitude of the deviation between the cracks is reduced with the increase of curvature. Systematic simulations show that both repulsive angle $\overline{\theta}_{\max}$ and the aspect ratio $\overline{H/W}$ decrease with the curvature (Fig. 11b), reflecting the shielding effects of curvature on the repulsive and attractive interaction of cracks on close cylindrical shells. Different from the configuration of the cylinder shell with zero Gaussian curvature K, we further explored the propagation of cracks on the curved configuration with nonzero Gaussian curvature. As shown in Fig. 11c, we simulated the complete trajectory of the crack pair on a flat sheet with a bump in the center, where the Gaussian curvature is positive on the top of the bump and negative on the outskirts of the bump. The simulated crack trajectories in Fig. 11d show that for cracks inclined with respect to the bump, the cracks repel each other at the onset of growth and then curve around the bump due to the interaction between cracks and the effects of curvature, forming a path composed of repulsive and attractive segments similar to that of cracks on flat sheets. Interestingly, the maximum repulsive angle $\theta_{\max}$ of two approaching cracks around the bump is significantly smaller than that of cracks on flat sheets, which also reflects the shielding effects of curvature on the repulsion between a pair of cracks. In summary, the shielding effect of curvature on the interaction of crack pairs is robust and universal, in a wide range of initial crack positions, material properties and curved configurations.

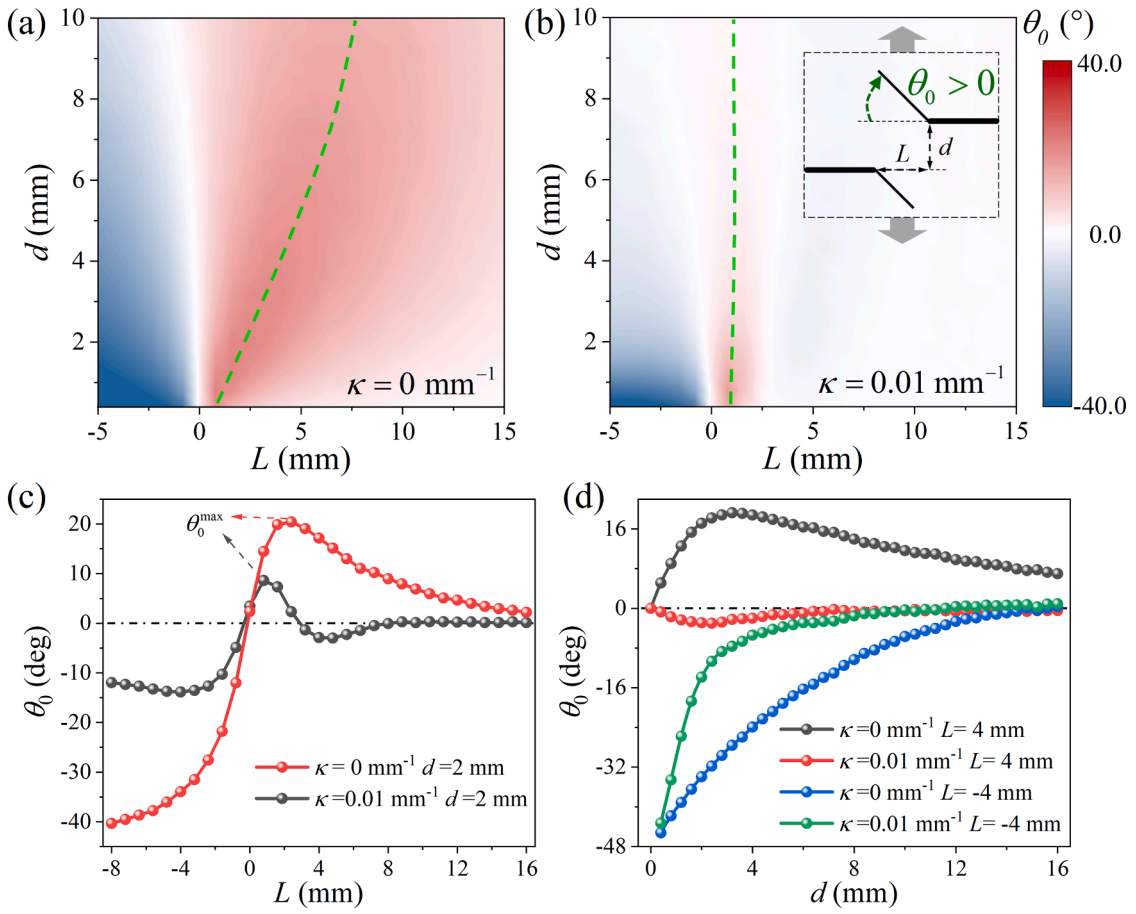

Fig. 12. Theoretical predictions for the evolution of the initial kink angles θ_0 of crack tips on (a) flat and (b) curved shells with different initial vertical distances d and horizontal distances L. The green dotted line represents the location of the local extremum of θ_0 ($\theta_0^{\max}$). (c) The variation of initial deflection angle of crack with L under different curvature κ. (d) The variation of initial deflection angle of crack with d under different κ and L.

4. Theoretical analysis

4.1. Theoretical method

We developed a theoretical model to study the effects of curvature on the interaction of cracks. For an open cylindrical shell with two parallel and offset cracks, in the coordinates of the crack tip (r,θ), the stress in the vicinity of the crack tip can be defined by the stress intensity factors K (Irwin et al., 1957)

$$\sigma_{ij} = K(2\pi r)^{-1/2} f_{ij}(\theta), \tag{4.1}$$

where K depends on external boundary conditions and the remaining parameters are only related to the spatial coordinates of the crack tips. We focused on a thin shell structure with negligible thickness. Therefore, the stress in the vicinity of the crack tip takes the form

$$\begin{Bmatrix} \sigma_{rr} \\ \sigma_{\theta\theta} \\ \tau_{r\theta} \end{Bmatrix} = \frac{K_{\mathrm{I}}}{\sqrt{2\pi r}} \begin{Bmatrix} \frac{5}{4}\cos\frac{\theta}{2} - \frac{1}{4}\cos\frac{3\theta}{2} \\ \frac{3}{4}\cos\frac{\theta}{2} + \frac{1}{4}\cos\frac{3\theta}{2} \\ \frac{1}{4}\cos\frac{\theta}{2} + \frac{1}{4}\sin\frac{3\theta}{2} \end{Bmatrix} + \frac{K_{\mathrm{II}}}{\sqrt{2\pi r}} \begin{Bmatrix} -\frac{5}{4}\sin\frac{\theta}{2} + \frac{3}{4}\sin\frac{3\theta}{2} \\ -\frac{3}{4}\sin\frac{\theta}{2} - \frac{3}{4}\sin\frac{3\theta}{2} \\ \frac{1}{4}\cos\frac{\theta}{2} + \frac{3}{4}\cos\frac{3\theta}{2} \end{Bmatrix}. \tag{4.2}$$

where the stress intensity factors K_I and K_{II} measure the intensity of tensile and shear stress concentration at the crack tip, respectively. Further. By considering the direction of the maximum hoop stress at the crack tip as the direction of crack propagation (Erdogan and Sih, 1963),

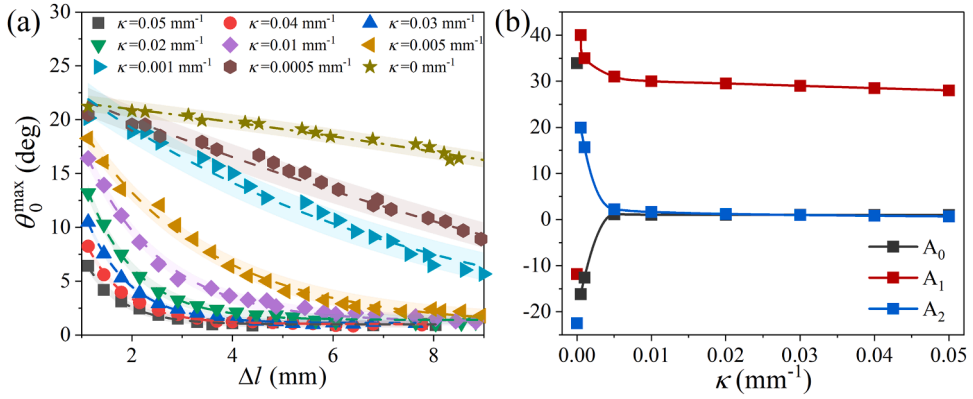

Fig. 13. (a) The relationship between $\theta_0^{\max}$ and $\Delta l = \sqrt{d^2 + L^2}$ with different curvature κ. (b) The relationship between the coefficients (A_0,A_1 and A_2) of the fitting formula and the curvature κ.

Table 1
Coefficients used in Eq. (4.6) for fitting the local maximum repulsion $\theta_0^{\max}$.

i	0	1	2
a_i	1.11763	29.3174	0.98866
b_i	−24.4184	19.5703	25.2528
c_i	0.00159	0.00082	0.00179

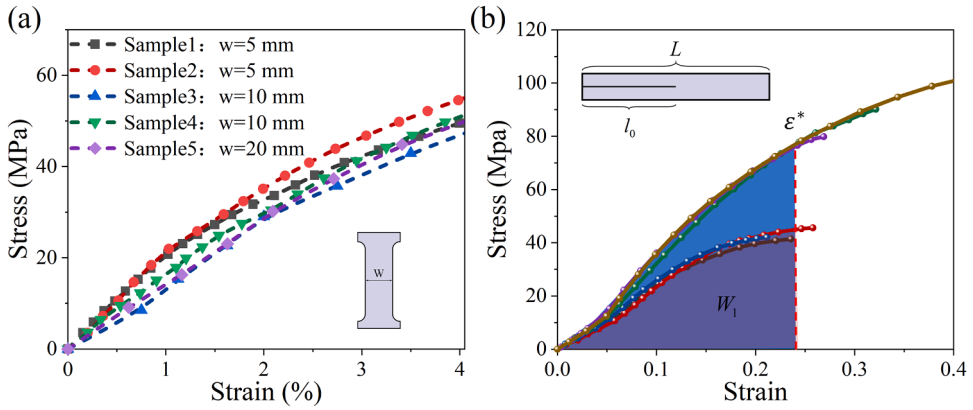

Fig. A1. Measurement of properties of experimental materials. (a) Stress-strain curves of uniaxial tension of samples with different widths, characterizing the elastic modulus E. (b) The fracture toughness G_c of the material was measured by the Rivlin-Thomas method (Rivlin and Thomas, 1953).

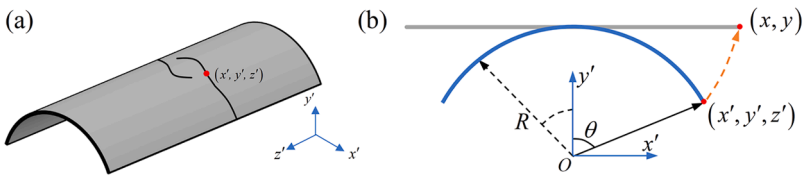

Fig. B1. (a) Coordinate of the crack on curved surface. (b) Transformation from 3D curved surface coordinates $(x^{'}, y^{'}, z^{'})$ to 2D plane coordinates (x, y). The origin of the x'-y' coordinate system O is located at the center of the arc. The blue line stands for the original surface, and the gray line stands for the converted plane.

$$\frac{\partial \sigma_{\theta\theta}(K_{\mathrm{I}}, K_{\mathrm{II}}, \theta)}{\partial \theta} = 0, \tag{4.3}$$

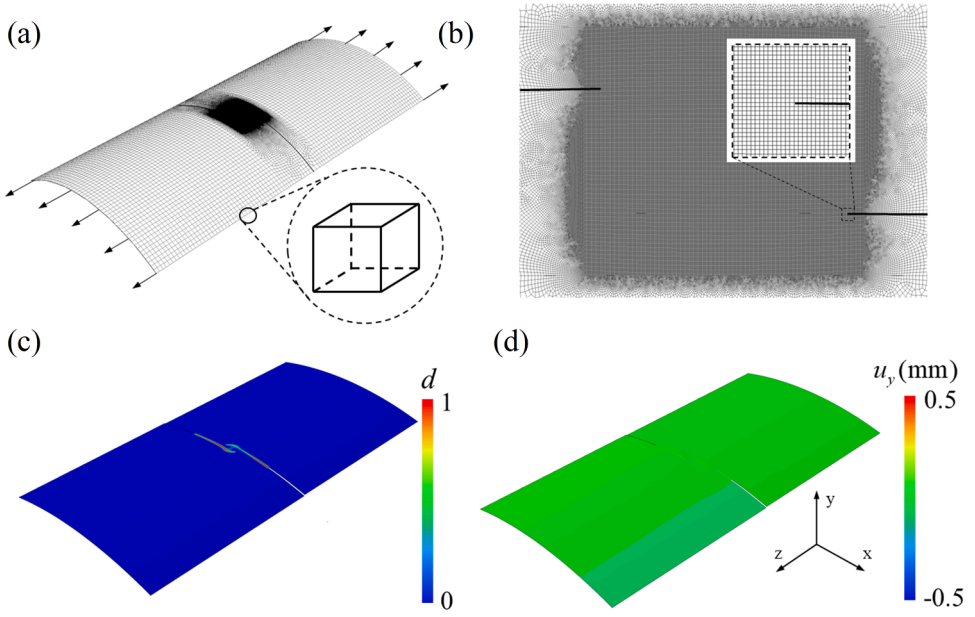

Fig. C1. (a) Division of fixed mesh in phase field fracture simulation. (b) Mesh subdivision of crack propagation region. (c) The simulation result of crack propagation. (d) The displacement in the y-direction after crack propagation.

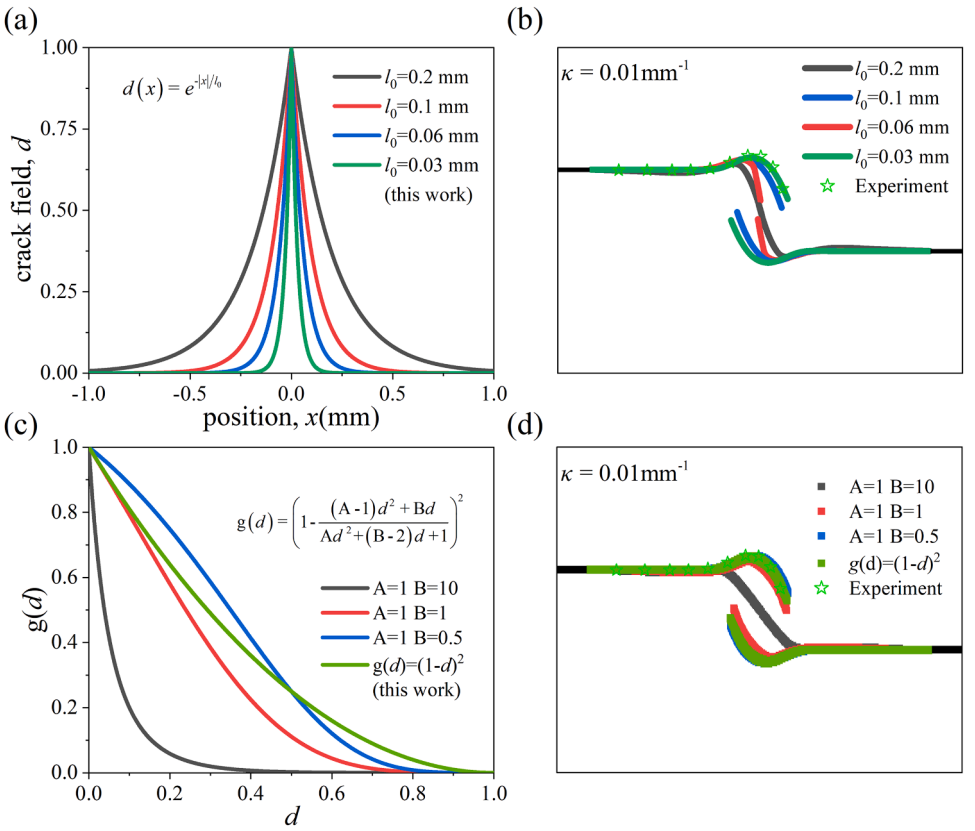

Fig. C2. Effects of phase-field parameters on the predicted crack trajectories. (a) Diffusive crack model described by phase field $d(x) = e^{-|x|/l_0}$ for different diffusive length l_0. (b) The predicted crack trajectories under different l_0. (c) The relationships between the degradation function $g(d)$ and the crack parameter d under different parameters. (d) The predicted crack trajectories under different $g(d)$.

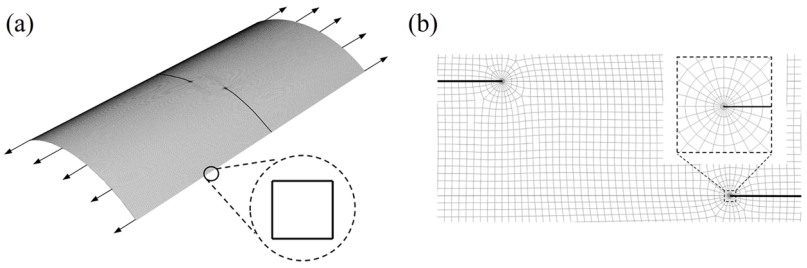

Fig. D1. Finite element mesh generation for the calculation of the stress intensity factors. (a) Division of fixed mesh in the calculation of stress intensity factor. (b) Mesh subdivision near the crack tips.

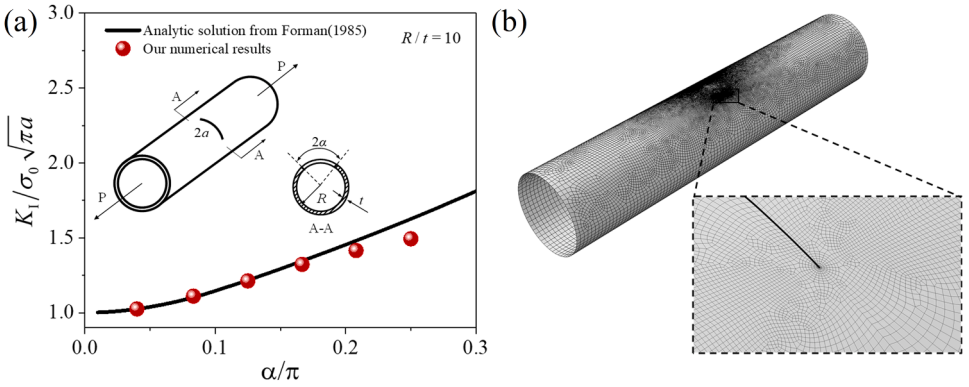

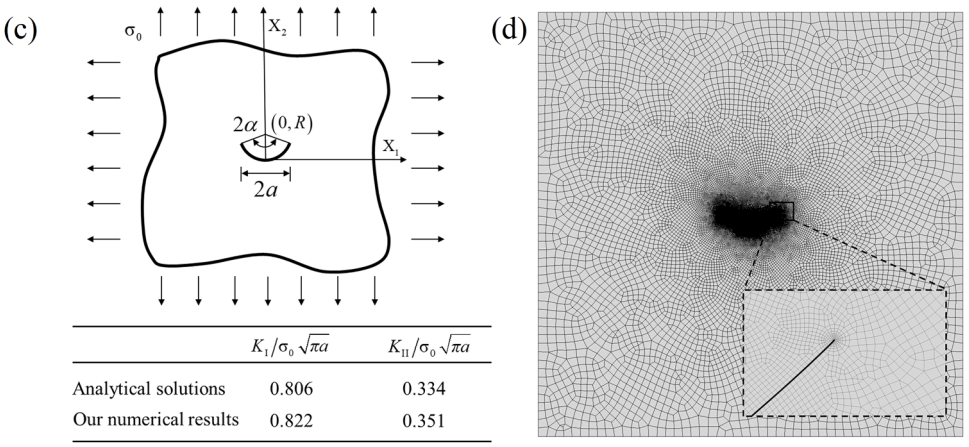

	$K_I/\sigma_0\sqrt{\pi a}$	$K_{II}/\sigma_0\sqrt{\pi a}$
Analytical solutions	0.806	0.334
Our numerical results	0.822	0.351

Fig. D2. Two benchmark problems for verifying the accuracy of the stress intensity factor at the crack tip. (a) Comparison of theoretical and numerical solutions for the stress intensity factors of a circumferential through-wall crack in a cylindrical shell. (b) The mesh of a circumferential through-wall crack in a cylindrical shell. (c) Comparison of numerical and analytical results for a 2D lens crack. (d) The mesh of a 2D lens crack.

the kink angle θ_0 at the onset of crack propagation can be described by the expression (Mitchell et al., 2017):

$$\theta_0 = 2\arctan\left[\frac{-2K_{II}/K_I}{1+\sqrt{1+8(K_{II}/K_I)^2}}\right], \tag{4.4}$$

where K_I and K_{II} depend on the curvature κ (see Appendix D), the initial horizontal distance L and the vertical distance d as shown in experiments. However, for the complex structure with multiple cracks with curvature, the traditional fracture mechanics theory cannot give the theoretical solution of K_I and K_{II}, but this can be easily determined in the finite element calculation through the well-known interaction integration program (see Appendix D). In addition, it's worth mentioning that we ignored the effects of K_{III}, due to the out-of-plane deformations are nearly zero (Fig. C1) and the crack tilt is mainly controlled by the mixed-mode I + II fracture rather than by

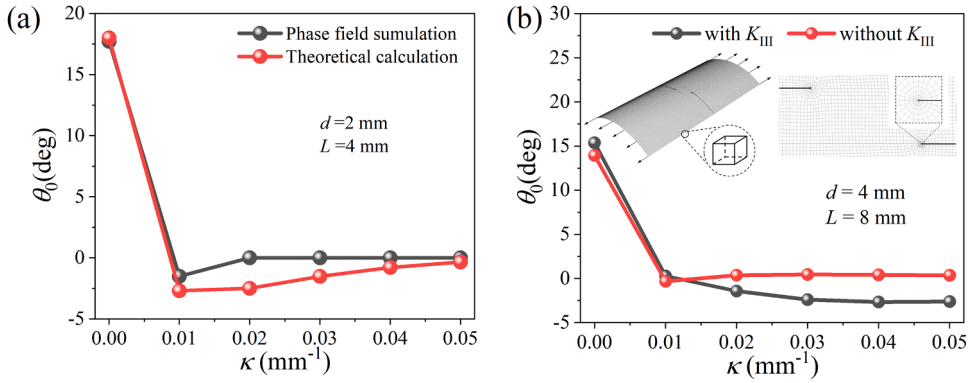

Fig. D3. (a) Comparison of theoretical and phase field numerical results for the initial deflection angle of cracks. (b) Comparison of the relationship between initial deflection angle and curvature with and without considering K_{III}.

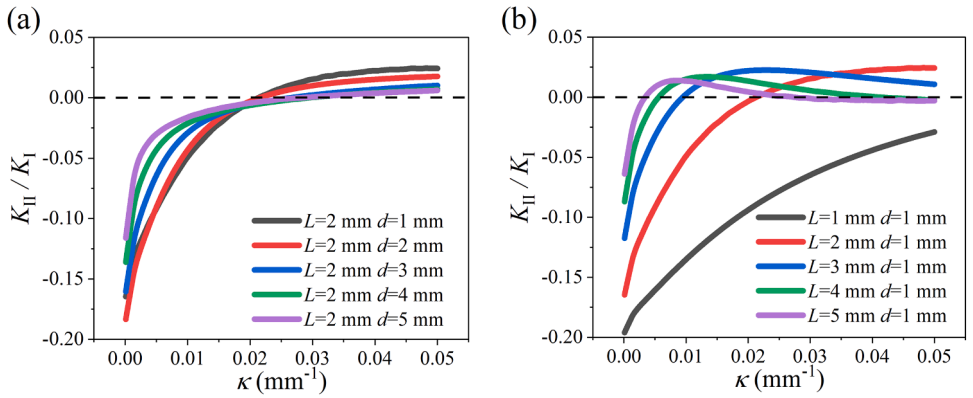

Fig. D4. The relationships between K_{II}/K_I and the curvature κ. (a) The calculated K_{II}/K_Iunder different d. (b) The calculated K_{II} $/K_I$under different L.

the mode III fracture in previous theoretical analysis (Mitchell et al., 2017; Schwaab et al., 2018). Meanwhile, results in Fig. D3b show that although there may be some numerical differences, the conclusion of the shielding effect of curvature on the interactions of a crack pair remains valid with considering K_{III}.

4.2. The effect of curvature on initial kink angle of cracks

By substituting the calculated K_I and K_{II} under different κ, L and d into Eq. (4.4), we plotted the initial kink angle θ_0 for a pair of cracks on plane and curved shell in the (d, L) space with strong crack interaction (Fig. 12a and 12b), where the sign of θ_0 indicates repulsion ($\theta_0 > 0$) and attraction ($\theta_0 < 0$). We found that the color in the phase diagram with curvature (Fig. 12b) is significantly lighter than that in the phase diagram without curvature (Fig. 12a), indicating the absolute values of θ_0 for cracks on curved shells are significantly lower than that for cracks on flat sheets, reflecting the shielding effect of curvature on the repulsive and attractive interactions between a pair of cracks. Meanwhile, we observed that when L decreases, i.e., two cracks get closer, two cracks repel each other, and θ_0 first increases and reaches a maximum initial repulsion angle θ_0^{max} (Fig. 12c) at a critical L, where the critical value of L decreases with increasing curvature. Then, θ_0 decreases acutely to less than zero as L further decreases ($L \leq 0$), and the two cracks begin to attract each other. Furthermore, when $L < 0$, for both on curved shells and plane cracks, as d decreases, the absolute values of θ_0 gradually increase until $d = 0$; however, when $L > 0$, the absolute values of θ_0 gradually increase until a certain value d and then decrease to zero until $d = 0$ (Fig. 12d). It is worth noting that the initial kink angle of crack tips under some (d, L) configurations will be transformed form negative to positive due to the effect of curvature, which provides some enlightenment for curvature-controlled crack patterns.

4.3. Effects of curvature on the local maxima of repulsion angle of cracks

Further, we found that the position of the local maxima of repulsion θ_0^{max} will change with different curvature, which means that the shielding effect of curvature on crack interactions is not only related to the spacing of crack pairs (d, L), but also related to the curvature

κ. Here, we paid close attention to the relationship between the local maxima of repulsion $\theta_0^{\max}$ and the tip-to-tip distance $\Delta l = \sqrt{d^2 + L^2}$ with different curvature κ, as shown in Fig. 13a. It can be clearly seen that the local maxima of repulsion $\theta_0^{\max}$ decreases with the increase of the distanceΔl, which can be fitted as an exponential function for different curvature:

$$\theta_0^{\max} = A_0 + A_1 e^{-\Delta l / A_2}. \tag{4.5}$$

The relationship of its coefficients (A_0, A_1 and A_2) with curvature is shown in Fig. 13b, which can be fitted as the exponential function of the curvature κ:

$$A_i = a_i + b_i \mathrm{e}^{-\kappa / c_i} (i = 0, 1, 2 \quad \kappa > 0), \tag{4.6}$$

where a_i, b_i and c_i are constants determined by numerical solutions (see Table 1).

Based on the fitted exponential scaling relationships of Eqs. (4.5) and (4.6), we can quantify the effects of the initial crack configurations $\Delta l = \sqrt{d^2 + L^2}$ and curvatures κ on the interaction of cracks. The exponentially decreasing function indicates that the crack interaction becomes weaker as the curvature and the crack tip-to-tip distance increase, i.e., the curvature can significantly shield the repulsive interaction between a pair of cracks. This exponential decreasing scaling relationship between the crack interaction and the curvature can be explained by the evolution of the direction of maximum principal stress (Fig. 8c), where the orientation angles of maximum principal stress decrease with increasing curvatures. Therefore, our developed semi-theoretical framework combining the finite element calculations and classic fracture mechanics is sufficient to quantitatively capture the complete crack trajectories and the shielding effects of curvature on the repulsion and attraction interaction of cracks.

5. Conclusion

In conclusion, in this paper we represented the universal shielding effect of curvature on the repulsive and attractive interactions of two approaching cracks, by developing a mechanical framework combining systematic experiments, simulations and fracture mechanics analysis. This shielding effect originates from the fact that the curvature can strongly modify the distribution and intensity of the singular stress field ahead of the crack tip and suppress the initial deflection angle of cracks. Considering different initial crack positions (initial vertical and horizontal distances between crack tips), material properties (elastic modulus and fracture toughness) and curved configurations (cylinder shell and bump), we found that the shielding effect of curvature on the interaction of cracks still exists. Systematic theoretical analyses built the laws to quantify how sensible interacting cracks are to the curvature and initial crack-tip distances. These results show the opportunity of using curvature as a novel means to guide the paths and the interaction of multiple cracks, with potential implications for controlling the cooperative fracture behaviors in thin films (Liu et al., 2022), flexible electronics (Rogers et al., 2010), mechanical sensors (Kang et al., 2014) and so on.

CRediT authorship contribution statement

Mengqi Liu: Investigation, Methodology, Software, Formal analysis, Data curation, Validation, Writing – original draft, Writing – review & editing. **Yu Zhen:** Investigation, Methodology, Writing – review & editing. **Yi Sun:** Investigation, Methodology, Writing – review & editing. **Linghui He:** Supervision, Investigation, Methodology, Writing – review & editing. **Kaijin Wu:** Investigation, Methodology, Formal analysis, Data curation, Validation, Funding acquisition, Writing – original draft, Writing – review & editing. **Yong Ni:** Conceptualization, Methodology, Supervision, Funding acquisition, Writing – review & editing.

Declaration of Competing Interest

The authors declare that they have no known competing financial interests or personal relationships that could have appeared to influence the work reported in this paper.

Data availability

Data will be made available on request.

Acknowledgments

This work was supported by the National Natural Science Foundation of China (Grant No. 12025206 and Grant No. 12202433), the National Postdoctoral Program for Innovative Talents (Grant No. BX2021284), the Nature Science Foundation of Anhui Province (Grant No. 2208085QA25), the USTC Research Funds of the Double First-Class Initiative (Grant No. YD2090002010) and the fellowship of China Postdoctoral Science Foundation (Grant No. 2022M723042). This work was partially carried out at the USTC Center for Micro and Nanoscale Research and Fabrication.

Appendix A. Measurement of properties of experimental materials

We used the Polyimide (PI) films in our experiments and measured three independent material parameters, the elastic modulus (E), the Poisson's ratio (ν), and the fracture toughness (G_c). We determined the elastic modulus (E) and Poisson's ratio (ν) by stretching a dog bone like samples through an instrument while recording images of the sample as it was strained (Fig. A1a). The stress-strain relationship of samples with different widths under uniaxial stress is obtained. By analyzing the image, the deformation of the edge is detected, and the nominal strain is used for measurement ν, which value is close to 0.5. We get an approximate value of the elastic modulus$E \approx 1.5 \pm 0.2$GPa. The third material parameter (G_c) is the energy required to create new surface, called fracture energy. We used a similar procedure proposed by Rivlin and Thomas (1953) and Mitchell et al. (2017). Pre-cut samples and uncut samples of the same geometry were strained very slowly (0.3 mm/min), and we recorded stress-strain curves in pure shear conditions in the instrument (Fig. A1b). This onset of crack growth for the pre-cut samples corresponds precisely to a maximum in the stress-strain curve (ε^*). The integral difference of the stress-strain curve for the pre-cut samples and uncut samples from $\varepsilon = 0$ to ε^* provides the elastic energy density W_0 far ahead of the crack at the moment the crack began to propagate. Hence, the fracture toughness $G_c = W_0 \cdot l_0 \approx 0.035 \pm 0.01$kN/mm, where l_0 is the seed crack length.

Appendix B. Transformation from curved surface to plane

In this paper, in order to compare the crack paths under different radii of curvature, we have carried out a simple coordinate transformation to project the crack coordinates on the surface onto the plane (Fig. B1):

$$x = \theta R = R\arctan(x^{'} / y^{'}), \tag{B.1}$$

$$y = z^{'}. \tag{B.2}$$

Appendix C. Phase-field numerical model

The phase field method in Section 3.1 is implemented into the commercial software ABAQUS through the user subroutine UEL (User-defined elements) (Molnár and Gravouil, 2017). As shown in Fig. C1a, in order to capture the evolution of two interacting initially parallel cracks more accurately, we finely divided the mesh of the crack propagation area. The finite element meshes of about 200, 000 3D solid elements with 8-nodes (C3D8) are used, and the region around the crack path is refined with the mesh size of 0.015 mm. In addition, it's worth mentioning that due to that the simulated out-of-plane deformations are nearly zero (Fig. C1d), we ignored the influences of wrinkles (Li et al., 2018; Feng et al., 2023), and we will further develop our numerical model in future to consider the coupling relationships between wrinkles and multiple cracks on curved structures. Meanwhile, due to the local out-of-plane deformation ($|u_y|_{max} / R \approx 10^{-2}$) is negligible at the repulsive and attractive stages, the local curved geometries are approximately consistent with the initial curved configuration during crack propagation.

In addition, we performed investigations on the effects of the diffusive length l_0 and the degradation function $g(d)$ on the predicted crack trajectories. As shown in Fig. C2a, l_0 is used to control the width of the regularized or diffusive crack (Miehe et al., 2010). As the l_0 decreases to $l_0 = 0.03$ mm, the calculated crack configuration tends to be stable and is in good agreement with experiments (Fig. C2b). Further, we analyzed the effects of the degradation function $g(d)$ on crack trajectories based a degradation function proposed by Cao et al. (2020):

$$g(d) = \left(1 - \frac{(A-1)d^2 + Bd}{Ad^2 + (B-2)d + 1}\right)^2 \tag{C.1}$$

where, parameter A and B control the degradation kinetics, as shown in Fig. C2c. As the parameter B (with a constant A) decreases, the evolution of degradation function with the damage parameter d becomes slow, and the calculated crack configuration tends to be stable (Fig. C2d). For simplicity, we used the degradation function $g(d) = (1-d)^2$ in our model, and the calculated crack configuration is stable and is in good agreement with experiments (Fig. C2d).

Appendix D. Calculations of stress intensity factors

In this paper, the calculation of stress intensity factor associated with initial deflection angle are realized by finite element (FE) software ABAQUS. To determine the initial kink angle (θ_0) of the crack via the maximum hoop stress criterion (Eq. (4.4)), we need to know the stress intensity factors (SIF). The SIF in the different curved configuration can be easily determined in a FE computation through the well-known interaction integral method, which separate and obtain K_{I} and K_{II} in the real field by establishing an auxiliary field at the crack tip (Stern et al., 1976). Since the stress, strain and displacement in linear elastic materials meet the superposition principle, the real field and auxiliary field can be superimposed into the J-integral formula:

$$J^s = \int_\Gamma \frac{1}{2}\left(\sigma_{ij} + \sigma_{ij}^{aux}\right)\left(\varepsilon_{ij} + \varepsilon_{ij}^{aux}\right)\delta_{1i}n_i ds - \int_\Gamma \left(\sigma_{ij} + \sigma_{ij}^{aux}\right)\left(u_{i,1} + u_{i,1}^{aux}\right)n_j ds = J^{real} + J^{aux} + I, \tag{D.1}$$

where J^{real} and J^{aux} are the J-integral of real field and auxiliary field, I is the coupling term:

$$I = \int_{\Gamma} \frac{1}{2}\left(\sigma_{ij}^{aux}\varepsilon_{ij}^{aux} + \sigma_{ij}^{aux}\varepsilon_{ij}\right)\delta_{1i}n_i ds - \int_{\Gamma}\left(\sigma_{ij}^{aux}u_{i,1}^{aux} + \sigma_{ij}^{aux}u_{i,1}\right)n_j ds. \tag{D.2}$$

In isotropic materials, the J-integral is related to strain energy release rate and stress intensity factor $J = G = \left(K_{\mathrm{I}}^2 + K_{\mathrm{II}}^2\right)/E$. Similarly, the J integral of the real field and the auxiliary field is:

$$J^S = \frac{1}{E}\left[\left(K_{\mathrm{I}} + K_{\mathrm{I}}^{aux}\right)^2 + \left(K_{\mathrm{II}} + K_{\mathrm{II}}^{aux}\right)^2\right] = J^{real} + J^{aux} + I, \tag{D.3}$$

$$I = \frac{2}{E}\left(K_{\mathrm{I}}K_{\mathrm{I}}^{aux} + K_{\mathrm{II}}K_{\mathrm{II}}^{aux}\right). \tag{D.4}$$

Substitute $K_{\mathrm{I}}^{aux} = 1$, $K_{\mathrm{II}}^{aux} = 0$ and $K_{\mathrm{I}}^{aux} = 0$, $K_{\mathrm{II}}^{aux} = 1$ into Eq. (D.2) and Eq. (D.4), through the calculation of two interaction integrals and we can get the stress intensity factor (K_{I} and K_{II}):

$$K_{\mathrm{I}} = \frac{E}{2}I\left(K_{\mathrm{I}}^{aux} = 1, K_{\mathrm{II}}^{aux} = 0\right), \tag{D.5}$$

$$K_{\mathrm{II}} = \frac{E}{2}I\left(K_{\mathrm{I}}^{aux} = 0, K_{\mathrm{II}}^{aux} = 1\right). \tag{D.6}$$

These formulas can be integrated into the finite element software ABAQUS to determine K_{I} and K_{II} under different curvature and crack-tip distances. The finite element meshes of about 100, 000 shell elements with 4-nodes (S4R) are used, we refined the mesh near the crack tips to ensure the convergence and accuracy of the calculation (Fig. D1c and D1d). Finally, K_{I} and K_{II} were determined for over 6000 (d, L, κ) combinations. This allowed us to explore the relationship between the initial deflection angle of the crack pair and the initial crack-tip distances with different curvatures.

In addition, to validate the accuracy of the stress intensity factor calculated by above methods, we constructed two calculated models to compare with theoretical results. As shown in Fig. D2a and D2b, we calculated the stress intensity factor of a circumferential through-wall curved crack with the angle $2\alpha$and arc length $2a$ in a cylindrical shell with the mean radius R, wall thickness t and length $2L$ under tensile force P. Results in Fig. D2a show that the stress intensity factor calculated by our model are in good agreement with previous theoretical results (Forman et al., 1985). Meanwhile, we constructed a model to calculate the stress intensity factor for a lens crack in an infinitely extended plate subjected to equiaxial tension, and the detailed geometries can be seen in Fig. D2c and D2d. As shown in Fig. D2c, the stress intensity factors calculated by our numerical model are in good agreement with the analytical solutions (Cotterell and Rice, 1980; Gosz and Moran, 2002; Muskhelishvili, 1953).

Besides, As shown in Fig. D3a, we have added a direct comparison between the theoretical results and the fully numerical ones (phase-field simulations). Under different curvatures, the values of initial deflection angles θ_0 simulated by phase-field modeling (Section 3) are in good agreement with that calculated by theoretical results (Section 4.1). Therefore, above results prove the accuracy of stress intensity factors calculated by our model in this work.

Furthermore, we calculated the ratio of stress intensity factors with different curvature κ under different vertical distances d and horizontal distances L. The results show the nonlinear relationships between the ratio of stress intensity factors $K_{\mathrm{II}}/K_{\mathrm{I}}$ and the curvature κ (Fig. D4). Further, by substituting these relationships into Eq. (4.4), we can calculate the initial deflection angles under different curvatures (Fig. 12), which reflects the shielding effects of the curvature on crack interactions.

References

Ambati, M., Gerasimov, T., De Lorenzis, L., 2015. A review on phase-field models of brittle fracture and a new fast hybrid formulation. Comput. Mech. 55, 383–405. https://doi.org/10.1007/s00466-014-1109-y.

Ball, P., 2016. Patterns in Nature: why the Natural World Looks the Way it Does. University of Chicago Press, Chicago. https://doi.org/10.7208/9780226332567.

Bausch, A., Bowick, M.J., Cacciuto, A., Dinsmore, A., Hsu, M., Nelson, D., Nikolaides, M., Travesset, A., Weitz, D., 2003. Grain boundary scars and spherical crystallography. Science 299, 1716–1718. https://doi.org/10.1126/science.1081160.

Bayart, E., Boudaoud, A., Adda-Bedia, M., 2011. Finite-distance singularities in the tearing of thin sheets. Phys. Rev. Lett. 106, 194301 https://doi.org/10.1103/PhysRevLett.106.194301.

Bourdin, B., Francfort, G.A., Marigo, J.J., 2000. Numerical experiments in revisited brittle fracture. J. Mech. Phys. Solids 48, 797–826. https://doi.org/10.1016/S0022-5096(99)00028-9.

Bourdin, B., Francfort, G.A., Marigo, J.J., 2008. The variational approach to fracture. J. Elast. 91, 5–148. https://doi.org/10.1007/s10659-007-9107-3.

Brau, F., 2014. Tearing of thin sheets: cracks interacting through an elastic ridge. Phys. Rev. E 90, 062406. https://doi.org/10.1103/PhysRevE.90.062406.

Cao, Y., Shen, W., Shao, J., Wang, W., 2020. A novel FFT-based phase field model for damage and cracking behavior of heterogeneous materials. Int. J. Plast. 133, 102786 https://doi.org/10.1016/j.ijplas.2020.102786.

Chen, X., Yin, J., 2010. Buckling patterns of thin films on curved compliant substrates with applications to morphogenesis and three-dimensional micro-fabrication. Soft Matter 6, 5667–5680. https://doi.org/10.1039/C0SM00401D.

Cotterell, B., Rice, J.R., 1980. Slightly curved or kinked cracks. Int. J. Fract. 16, 155–169. https://doi.org/10.1007/BF00012619.

Coupeau, C., Boijoux, R., Ni, Y., Parry, G., 2019. Interacting straight-sided buckles: an enhanced attraction by substrate elasticity. J. Mech. Phys. Solids 124, 526–535. https://doi.org/10.1016/j.jmps.2018.11.010.

Dalbe, M.J., Koivisto, J., Vanel, L., Miksic, A., Ramos, O., Alava, M., Santucci, S., 2015. Repulsion and attraction between a pair of cracks in a plastic sheet. Phys. Rev. Lett. 114, 205501 https://doi.org/10.1103/PhysRevLett.114.205501.

Erdogan, F., Sih, G.C., 1963. On the crack extension in plates under plane loading and transverse shear. J. Fluids. Eng. 85, 519–525. https://doi.org/10.1115/1.3656897.
Fender, M.L., Lechenault, F., Daniels, K.E., 2010. Universal shapes formed by two interacting cracks. Phys. Rev. Lett. 105, 125505 https://doi.org/10.1103/PhysRevLett.105.125505.
Feng, S., Wang, W., Wang, S., Cui, X., Yang, Y., Xu, F., Liu, L., Xu, Z., 2023. Controlling and visualizing fracture of 2D crystals by wrinkling. J. Mech. Phys. Solids 174, 105253. https://doi.org/10.1016/j.jmps.2023.105253.
Folias, E.S., 1969. On the effect of initial curvature on cracked flat sheets. Int. J. Frac. Mech. 5, 327–346. https://doi.org/10.1007/BF00190962.
Forman, R.G., Hickman, J.C., Shivaskumar, V., 1985. Stress intensity factors for circumferential through cracks in hollow cylinders subjected to combined tension and bending loads. Eng. Fract. Mech. 21, 563–571. https://doi.org/10.1016/S0013-7944(85)80049-7.
Francfort, G.A., Marigo, J.J., 1998. Revisiting brittle fracture as an energy minimization problem. J. Mech. Phys. Solids 46, 1319–1342. https://doi.org/10.1016/S0022-5096(98)00034-9.
Fuentealba, J.F., Hamm, E., Roman, B., 2016. Intertwined multiple spiral fracture in perforated sheets. Phys. Rev. Lett. 116, 165501 https://doi.org/10.1103/PhysRevLett.116.165501.
Ghelichi, R., Kamrin, K., 2015. Modeling growth paths of interacting crack pairs in elastic media. Soft Matter 11, 7995–8012. https://doi.org/10.1039/C5SM01376C.
Goehring, L., Nakahara, A., Dutta, T., Kitsunezaki, S., Tarafdar, S., 2015. Desiccation Cracks and their Patterns: Formation and Modelling in Science and Nature. John Wiley & Sons.
Gosz, G., Moran, B., 2002. An interaction energy integral method for computation of mixed-mode stress intensity factors along non-planar crack fronts in three dimensions. Eng. Fract. Mech. 69, 299–319. https://doi.org/10.1016/S0013-7944(01)00080-7.
Guerra, R.E., Kelleher, C.P., Hollingsworth, A.D., Chaikin, P.M., 2018. Freezing on a sphere. Nature 554, 346–350. https://doi.org/10.1038/nature25468.
Hamm, E., Reis, P., LeBlanc, M., Roman, B., Cerda, E., 2008. Tearing as a test for mechanical characterization of thin adhesive films. Nat. Mater. 7, 386–390. https://doi.org/10.1038/nmat2161.
Han, Z., Qian, C., Tang, L., Li, H., 2019. Determination of the enhancement or shielding interaction between two parallel cracks under fatigue loading. Materials 12, 1331. https://doi.org/10.3390/ma12081331.
Irvine, W., Vitelli, V., Chaikin, P.M., 2010. Pleats in crystals on curved surfaces. Nature 468, 947–951. https://doi.org/10.1038/nature09620.
Irwin, G.R., 1957. Analysis of stresses and strains near the end of a crack traversing a plate. J. Appl. Mech. 24, 361–364. https://doi.org/10.1115/1.4011547.
Jeong, H., Signetti, S., Han, T.S., Ryu, S., 2018. Phase field modeling of crack propagation under combined shear and tensile loading with hybrid formulation. Comput. Mater. Sci. 155, 483–492. https://doi.org/10.1016/j.commatsci.2018.09.021.
Jiménez, F.L., Stoop, N., Lagrange, R., Dunkel, J., Reis, P.M., 2016. Curvature-controlled defect localization in elastic surface crystals. Phys. Rev. Lett. 116, 104301 https://doi.org/10.1103/PhysRevLett.116.104301.
Kachanov, M., 1993. Elastic solids with many cracks and related problems. Adv. Appl. Mech. 30, 259–445. https://doi.org/10.1016/S0065-2156(08)70176-5.
Kamrin, K., 2017. Cracks by design. Nat. Mater. 16, 8–9. https://doi.org/10.1038/nmat4831.
Kang, D., 2014. Ultrasensitive mechanical crack-based sensor inspired by the spider sensory system. Nature 516, 222–226. https://doi.org/10.1038/nature14002.
Klein, Y., Sharon, E., 2021. Buckling-fracture transition and the geometrical charge of a crack. Phys. Rev. Lett. 127, 105501 https://doi.org/10.1103/PhysRevLett.127.105501.
Koivisto, J., Dalbe, M.J., Alava, M., Santucci, S., 2016. Path (un) predictability of two interacting cracks in polycarbonate sheets using digital image correlation. Sci. Rep. 6, 32278. https://doi.org/10.1038/srep32278.
Kranz, R.L., 1979. Crack-crack and crack-pore interactions in stressed granite. Int. J. Rock Mech. Min. Sci. & Geomech. Abstr. 16, 37–47. https://doi.org/10.1016/0148-9062(79)90773-3.
Kruglova, O., Brau, F., Villers, D., Damman, P., 2011. How geometry controls the tearing of adhesive thin films on curved surfaces. Phys. Rev. Lett. 107, 164303 https://doi.org/10.1103/PhysRevLett.107.164303.
Li, S., Yu, S., He, L., Ni, Y., 2018. Effects of ridge cracking and interface sliding on morphological symmetry breaking in straight-sided blisters. J. Mech. Phys. Solids 112, 637–649. https://doi.org/10.1016/j.jmps.2017.10.001.
Liu, M., Yu, S., He, L., Ni, Y., 2022. Recent progress on crack pattern formation in thin films. Soft Matter 18, 5906–5927. https://doi.org/10.1039/D2SM00716A.
Liu, Z.E., Wei, Y., 2021. An analytical solution to the stress fields of kinked cracks. J. Mech. Phys. Solids 156, 104619. https://doi.org/10.1016/j.jmps.2021.104619.
Marthelot, J., Bico, J., Melo, F., Roman, B., 2015. A new failure mechanism in thin film by collaborative fracture and delamination: interacting duos of cracks. J. Mech. Phys. Solids 84, 214–229. https://doi.org/10.1016/j.jmps.2015.07.010.
Marthelot, J., Roman, B., Bico, J., Teisseire, J., Dalmas, D., Melo, F., 2014. Self-replicating cracks: a collaborative fracture mode in thin films. Phys. Rev. Lett. 113, 085502 https://doi.org/10.1103/PhysRevLett.113.085502.
Martins, A.F., Bennett, N.C., Clavel, S., Groenewald, H., Hensman, S., Hoby, S., Joris, A., Manger, P.R., Milinkovitch, M.C., 2018. Locally-curved geometry generates bending cracks in the African elephant skin. Nat. Commun. 9, 3865. https://doi.org/10.1038/s41467-018-06257-3.
Melin, S., 1983. Why do cracks avoid each other? Int. J. Fract. 23, 37–45. https://doi.org/10.1007/BF00020156.
Meng, G., Paulose, J., Nelson, D.R., Manoharan, V.N., 2014. Elastic instability of a crystal growing on a curved surface. Science 343, 634–637. https://doi.org/10.1126/science.1244827.
Miehe, C., Hofacker, M., Welschinger, F., 2010. A phase field model for rate-independent crack propagation: robust algorithmic implementation based on operator splits. Comput. Methods Appl. Mech. Eng. 199, 2765–2778. https://doi.org/10.1016/j.cma.2010.04.011.
Mitchell, N.P., Koning, V., Vitelli, V., Irvine, W.T., 2017. Fracture in sheets draped on curved surfaces. Nat. Mater. 16, 89–93. https://doi.org/10.1038/nmat4733.
Molnár, G., Gravouil, A., 2017. 2D and 3D Abaqus implementation of a robust staggered phase-field solution for modeling brittle fracture. Finite Elem. Anal. Des. 130, 27–38. https://doi.org/10.1016/j.finel.2017.03.002.
Muskhelishvili N.I., 1953. Some basic problems in the mathematical theory of elasticity. Leiden: Noordhoff. 10.1017/S1446788700004535.
Ni, Y., Soh, A.K., 2014. On the growth of buckle-delamination pattern in compressed anisotropic thin films. Acta Mater. 69, 37–46. https://doi.org/10.1016/j.actamat.2014.01.041.
Pons, A.J., Karma, A., 2010. Helical crack-front instability in mixed-mode fracture. Nature 464, 85–89. https://doi.org/10.1038/nature08862.
Rivlin, R.S., Thomas, A.G., 1953. Rupture of rubber. I. Characteristic energy for tearing. J. Polym Sci. 10, 291–318. https://doi.org/10.1002/pol.1953.120100303.
Rogers, J.A., Someya, T., Huang, Y., 2010. Materials and mechanics for stretchable electronics. Science 327, 1603–1607. https://doi.org/10.1126/science.1182383.
Schwaab, M.-É., 2018. Croissance de fissures en interaction: étude numérique du cas “En passant”. Material chemistry. Université de Lyon. English.
Schwaab, M.É., Biben, T., Santucci, S., Gravouil, A., Vanel, L., 2018. Interacting cracks obey a multiscale attractive to repulsive transition. Phys. Rev. Lett. 120, 255501 https://doi.org/10.1103/PhysRevLett.120.255501.
Seelig, T., Gross, D., 1999. On the interaction and branching of fast running cracks—A numerical investigation. J. Mech. Phys. Solids 47, 935–952. https://doi.org/10.1016/S0022-5096(98)00069-6.
Song, Z., Mu, X., Luo, T., Xu, Z., 2016. Unzipping of carbon nanotubes is geometry-dependent. Nanotechnology 27, 015601. https://iopscience.iop.org/article/10.1088/0957-4484/27/1/015601.
Song, Z., Ni, Y., Xu, Z., 2017. Geometrical distortion leads to Griffith strength reduction in graphene membranes. Extreme Mech. Lett. 14, 31–37. https://doi.org/10.1016/j.eml.2017.01.005.
Stern, M., Becker, E.B., Dunham, R.S., 1976. A contour integral computation of mixed-mode stress intensity factors. Int. J. Fract. 12, 359–368. https://doi.org/10.1007/BF00032831.
Tobasco, I., Timounay, Y., Todorova, D., Leggat, G.C., Paulsen, J.D., Katifori, E., 2022. Exact solutions for the wrinkle patterns of confined elastic shells. Nat. Phys. 18, 1099–1104. https://doi.org/10.1038/s41567-022-01672-2.
Vattré, A., 2022. Kinked and forked crack arrays in anisotropic elastic bimaterials. J. Mech. Phys. Solids 160, 104744. https://doi.org/10.1016/j.jmps.2021.104744.

Wang, L., Ji, X.Y., Wang, N., Wu, J., Dong, H., Du, J., Zhao, Y., Feng, X.Q., Jiang, L., 2012. Biaxial stress controlled three-dimensional helical cracks. NPG Asia Mater. 4, e14. https://doi.org/10.1038/am.2012.26.

Wang, T., Dai, Z., Potier-Ferry, M., Xu, F., 2023. Curvature-regulated multiphase patterns in Tori. Phys. Rev. Lett. 130, 048201 https://doi.org/10.1103/PhysRevLett.130.048201.

Wang, T., Yang, Y., Fu, C., Liu, F., Wang, K., Xu, F., 2020. Wrinkling and smoothing of a soft shell. J. Mech. Phys. Solids 134, 103738. https://doi.org/10.1016/j.jmps.2019.103738.

Wu, J.Y., Nguyen, V.P., Nguyen, C.T., Sutula, D., Sinaie, S., Bordas, S.P., 2020. Phase-field modeling of fracture. Adv. Appl. Mech. 53, 1–183. https://doi.org/10.1016/bs.aams.2019.08.001.

Xu, F., Potier-Ferry, M., 2016. On axisymmetric/diamond-like mode transitions in axially compressed core–shell cylinders. J. Mech. Phys. Solids 94, 68–87. https://doi.org/10.1016/j.jmps.2016.04.025.

Yao, H., Zhang, C., 2022. A generalized solution to the combo-crack problem—I. Pressure load on crack surface. J. Mech. Phys. Solids 159, 104783. https://doi.org/10.1016/j.jmps.2022.104783.

Yao, H., Zhang, C., 2022. A generalized solution to the combo-crack problem—II. Remote load. J. Mech. Phys. Solids 164, 104919. https://doi.org/10.1016/j.jmps.2022.104919.

Yu, S.J., Shi, Y.C., Chen, M.G., Si, P.Z., Zhou, Y., Zhang, X.F., Chen, J., Zhou, H., Jiao, Z.W., 2013. Coalescence behaviors of telephone cord buckles in SiAlNx films. Surf. Coat. Technol. 232, 884–890. https://doi.org/10.1016/j.surfcoat.2013.06.117.

Yuse, A., Sano, M., 1993. Transition between crack patterns in quenched glass plates. Nature 362, 329–331. https://doi.org/10.1038/362329a0.

Zeng, X., Wei, Y., 2016. The influence of crack-orientation distribution on the mechanical properties of pre-cracked brittle media. Int. J. Solids Struct. 96, 64–73. https://doi.org/10.1016/j.ijsolstr.2016.06.022.

Zhao, Y., Zhu, H., Jiang, C., Cao, Y., Feng, X.Q., 2020. Wrinkling pattern evolution on curved surfaces. J. Mech. Phys. Solids 135, 103798. https://doi.org/10.1016/j.jmps.2019.103798.